

A Bayesian Approach to Estimating Background Flows from a Passive Scalar

Jeff Borggaard, Nathan E. Glatt-Holtz, Justin A. Krometis

emails: jborggaard@vt.edu, negh@tulane.edu, jkrometis@vt.edu

Abstract

We consider the statistical inverse problem of estimating a background flow field (e.g., of air or water) from the partial and noisy observation of a passive scalar (e.g., the concentration of a solute), a common experimental approach to visualizing complex fluid flows. Here the unknown is a vector field that is specified by a large or infinite number of degrees of freedom. Since the inverse problem is ill-posed, i.e., there may be many or no background flows that match a given set of observations, we adopt a Bayesian approach to regularize it. In doing so, we leverage frameworks developed in recent years for infinite-dimensional Bayesian inference. The contributions in this work are threefold. First, we lay out a functional analytic and Bayesian framework for approaching this problem. Second, we define an adjoint method for efficient computation of the gradient of the log likelihood, a key ingredient in many numerical methods. Finally, we identify interesting example problems that exhibit posterior measures with simple and complex structure. We use these examples to conduct a large-scale benchmark of Markov Chain Monte Carlo methods developed in recent years for infinite-dimensional settings. Our results indicate that these methods are capable of resolving complex multimodal posteriors in high dimensions.

Keywords: Bayesian Statistical Inversion, Markov Chain Monte Carlo (MCMC), Passive Scalars, Fluid Turbulence

Contents

1	Introduction	2
2	Mathematical Framework and Bayesian Inference	4
3	Computational Approach and Challenges	7
4	Numerical Experiments: Posterior Complexity and MCMC Convergence	10
A	Selected Numerical Results for the IS and MALA Algorithms	21
B	Convergence of Observables	23
C	A General Setting for Bayes' Theorem	26
	References	29

1 Introduction

A common approach to investigating complex fluid flows is through measurement of a substance moving within the fluid. For example, dye, smoke, or neutrally-buoyant particles are injected into fluids to visualize vortices or other structures in turbulent flows [32, 33, 56, 48]. In this work we consider the inverse problem of estimating a background fluid flow from partial, noisy observations of a dye, pollutant, or other solute advecting and diffusing within the fluid. The initial condition is assumed to be known, so the problem can be interpreted as a controlled experiment, where a substance is added at known locations and then observed as the system evolves to investigate the structure of the underlying flow.

The physical model considered is the two-dimensional advection-diffusion equation on the periodic domain $\mathbb{T}^2 = [0, 1]^2$:

$$\frac{\partial}{\partial t}\theta(t, \mathbf{x}) = -\mathbf{v}(\mathbf{x}) \cdot \nabla\theta(t, \mathbf{x}) + \kappa\Delta\theta(t, \mathbf{x}) \quad , \quad \theta(0, \mathbf{x}) = \theta_0(\mathbf{x}). \quad (1.1)$$

Here

- $\theta : \mathbb{R}^+ \times \mathbb{T}^2 \rightarrow \mathbb{R}$ is a *passive scalar*, typically the concentration of some solute of interest, which is spread by diffusion and the motion of a (time-stationary) fluid flow \mathbf{v} . This solute is “passive” in that it does not affect the motion of the underlying fluid.
- $\mathbf{v} : \mathbb{T}^2 \rightarrow \mathbb{R}^2$ is an *incompressible background flow*, i.e., \mathbf{v} is constant in time and satisfies $\nabla \cdot \mathbf{v} = 0$.
- $\kappa > 0$ is the *diffusion coefficient*, which models the rate at which local concentrations of the solute spread out within the solvent in the absence of advection.

We obtain finite observations $\mathcal{Y} \in Y$ (e.g., \mathbb{R}^N or \mathbb{C}^N) subject to additive noise η , i.e.

$$\mathcal{Y} = \mathcal{G}(\mathbf{v}) + \eta \quad , \quad \eta \sim \gamma_0 \quad (1.2)$$

for some measure γ_0 related to the precision of the observations. Here, $\mathcal{G} : H \rightarrow Y$ is the *parameter-to-observable*, or forward, map. This \mathcal{G} associates the background flow \mathbf{v} , sitting in a suitable function space H , with a finite collection of measurements (observables) of the resulting $\theta = \theta(\mathbf{v})$. The observations may take a number of forms, such as:

- Spatial-temporal point observations: $\mathcal{G}_j(\mathbf{v}) = \theta(t_j, \mathbf{x}_j, \mathbf{v})$ for $t_j \in [0, T]$ and $\mathbf{x}_j \in [0, 1]^2$.
- Spectral components: $\mathcal{G}_j(\mathbf{v}) = \langle \theta(t_j, \cdot, \mathbf{v}), \mathbf{e}_{\mathbf{k}_j} \rangle_{L^2(\mathbb{T}^2)}$ for some basis $\{\mathbf{e}_{\mathbf{k}}\}$ of the scalar field θ .
- Local averages: $\mathcal{G}_j(\mathbf{v}) = \frac{1}{|\mathcal{D}_j|} \int_{\mathcal{D}_j} \theta(t, \mathbf{x}, \mathbf{v}) d\mathbf{x} dt$, for sub-domains $\mathcal{D}_j \subset [0, T] \times [0, 1]^2$ where $|\mathcal{D}_j|$ denotes the volume of \mathcal{D}_j .
- Other physical quantities of interest from θ , such as variance, dissipation rate, or structure functions.

This work will focus on point observations as the most obvious practical implementation. However, we note that the methodology outlined in this manuscript is quite general. Moreover, while we have assumed a divergence-free flow, point observations, and periodic boundary conditions, the framework herein could be adapted to other assumptions via a different definition of the forward map \mathcal{G} .

As we illustrate below, the proposed inverse problem is ill-posed, i.e., there may be many or no background flows \mathbf{v} that match a given dataset \mathcal{Y} . To address this issue, we adopt a Bayesian approach, incorporating prior knowledge of background flows and descriptions of the observation error to develop probabilistic estimates of \mathbf{v} . Summaries of the Bayesian approach to inverse problems can be found in [21] and [31]. Moreover, since the target of the inversion, the background flow \mathbf{v} , is infinite-dimensional, this work will leverage the considerable amount of recent research in infinite-dimensional Bayesian inference, grounding much of our approach in the overview of the field provided in [16]. To compute observables, such as the mean, variance, or (normalized) histogram of a given quantity on \mathbf{v} or θ , we use recently-developed Metropolis-Hastings Markov Chain Monte Carlo (MCMC) algorithms that are well-defined in infinite dimensions. We focus on preconditioned Crank-Nicolson (pCN) [14] and Hamiltonian (or Hybrid) Monte Carlo (HMC) [4] samplers; some results for the independence sampler and Metropolis-adjusted Langevin (MALA) methods (see descriptions in, e.g., [16] and [3], respectively) are provided in the appendices.

This work makes a number of important contributions. We lay out a Bayesian framework for the estimation of divergence-free background flows from observations of scalar behavior, a common experimental approach to investigating complex fluid flows [32, 33, 56, 48]. We define, prove, and numerically implement an adjoint method for the efficient computation of the gradient of the log likelihood, a key ingredient in higher-order MCMC methods. Finally, we identify two interesting examples for which the resulting posterior measures have very different structures - one fairly simple and one highly multi-modal. We use these two examples to conduct a systematic, large-scale numerical study to benchmark the convergence of the MCMC methods mentioned above for “easy” and “hard” problems. This is a companion paper to [9], where we investigate the behavior of the posterior measure as the number of point observations grows large (see also [38]), and [10], where we identify a computationally-efficient approach to computing the forward map.

The structure of the paper is as follows. [Section 2](#) defines our parametrization of the space of divergence-free flows, describes why the inverse problem is ill-posed in the traditional sense, and presents the Bayesian approach to the inverse problem. [Section 3](#) describes the numerical approach to computing the posterior measure: MCMC methods for sampling from the posterior, numerical methods for solving the advection-diffusion equation (1.1), and an adjoint method for computing the gradients required for some MCMC methods. [Section 4](#) provides results of the inference and convergence of MCMC methods as applied to two example problems. For completeness, appendices provide additional numerical results ([Appendix A](#) and [Appendix B](#)) and a description of Bayesian inference in a very general setting ([Appendix C](#)).

1.1 Literature Review

Bayesian Inference and MCMC Comprehensive overviews of modern Bayesian techniques, from the basics of probability theory to computational practicalities, can be found in [21] and [31]. In the last ten years, much attention has been paid to development of the theory of Bayesian inference for infinite-dimensional problems (e.g., where the target of the inversion is a function). These advances are summarized in [16], building upon the work in [49]; we follow the former closely in [Section 2](#) and provide a somewhat more general derivation of Bayes’ Theorem in [Appendix C](#).

Similarly, while Metropolis-Hastings Markov Chain Monte Carlo (MCMC) methods date to the foundational works [41] and [28], substantial recent work has gone into extending these methods to problems where the space to be sampled is high- or infinite-dimensional [5, 6, 7]. The goal of these efforts has been to define sampling kernels that are both well-defined and yield robust convergence even as the number of dimensions to be sampled grows large. The extension of Metropolis-Hastings methods to generalized state spaces was described in [52]. The behavior of the traditional random walk approach as the dimension grows large was investigated in [40] for a broad class of target measures. The pCN and MALA algorithms suitable for infinite-dimensional problems were laid out in [14]; the optimal choice of the step size parameter in the MALA algorithm was shown in [44]. HMC was similarly extended to infinite-dimensions in [4], work that was later generalized in [3] and [22]. Dimension-independent convergence of some of the above methods has been investigated by showing that the kernels have spectral gaps [20, 27, 53], leveraging a generalized version of Harris’ Theorem [24, 26, 25, 42] for Markov kernels. The work in [Section 4](#) represents one of the first attempts to benchmark these methods for an infinite-dimensional application.

In [Section 4.2](#) we present a multimodal posterior measure, which MCMC methods have difficulty resolving. This has been a known problem with MCMC almost since its inception and a number of ideas have been proposed for improving sampling for these distributions. One example is tempering, in which a series of “less steep” distributions are used to try to increase the probability of jumps between modes; see, e.g., the description in [21, Section 12.3] and associated references. A related method is equi-energy sampling [34], in which rings of parameter values associated with different energy levels are constructed and samples are allowed to jump within rings.

Advection-Diffusion The problem of observing scalar behavior to infer the underlying velocity field is a common experimental approach for investigating the structure of complex fluid flows. The textbooks [56] and [48] describe many such methods, including examples where dye, smoke, temperature, hydrogen bubbles, or photo-sensitive tracers are used. An overview of dye-based visualization techniques is provided in [32]. An application of dye to investigate two-dimensional turbulence is described in [55]; see the survey article [33] for additional examples.

To our knowledge, this work is the first to apply Bayesian inference to the problem of estimating a background fluid flow from measurements of a passive scalar. However, a number of works, such as [1], have used inversion techniques to determine a source (forcing) term in advection-diffusion problems. In those previous works, the background flow was assumed to be known and the initial condition assumed to be zero; their goal was to determine the function (in particular the location) from which the pollutant was dispersed. The source-identification work was extended to ensure robustness to uncertainties in the velocity field in [57].

More generally, the advection and diffusion of passive scalars has been studied extensively. Numerical difficulties in modeling the behavior of passive scalars for advection-dominated cases are described in [43] and [50]. Passive scalars exhibit similar behavior for turbulent and random flows, so the latter, simpler case may be used to model the former. One such model was introduced by Kraichnan [35, 36, 37]; the energy spectrum from this model motivates the construction of the prior measure in Section 4.

2 Mathematical Framework and Bayesian Inference

In this section, we describe the mathematical framework of the inverse problem (1.2). We begin by defining the functional analytic setting for the problem, including how we represent divergence-free background flows. We then describe reasons why the inverse problem is ill-posed, i.e., why a given set of measurements \mathcal{Y} cannot identify a unique background flow \mathbf{v} that generated them. We close the section by defining the Bayesian approach to the inverse problem.

2.1 Representation of Divergence-Free Background Flows

The target of the inference is a divergence-free background flow \mathbf{v} , so we start by describing the space H of such flows that we will consider. For this purpose we begin by recalling the Sobolev spaces of (scalar valued) periodic functions on the domain $\mathbb{T}^2 = [0, 1]^2$

$$H^s(\mathbb{T}^2) = \left\{ u : u = \sum_{\mathbf{k} \in \mathbb{Z}^2 \setminus \{0\}} c_{\mathbf{k}} e^{2\pi i \mathbf{k} \cdot \mathbf{x}}, \overline{c_{\mathbf{k}}} = c_{-\mathbf{k}}, \|u\|_{H^s} < \infty \right\}, \|u\|_{H^s}^2 := \sum_{\mathbf{k} \in \mathbb{Z}^2} \|\mathbf{k}\|^{2s} |c_{\mathbf{k}}|^2, \quad (2.1)$$

defined for any $s \in \mathbb{R}$; see e.g. [46, 51]. We will abuse notation and use the same notation for periodic divergence-free background flows by replacing the coefficients $c_{\mathbf{k}}$ in (2.1) with

$$c_{\mathbf{k}} = v_{\mathbf{k}} \frac{\mathbf{k}^\perp}{\|\mathbf{k}\|_2}, \quad \overline{v_{\mathbf{k}}} = -v_{-\mathbf{k}}, \quad (2.2)$$

where $\mathbf{k}^\perp = [-k_y, k_x]$ to ensure $\mathbf{k} \cdot \mathbf{k}^\perp = 0$. Throughout what follows we fix our parameter space as

Notation 2.1 (Parameter space, H). *We consider background flows $\mathbf{v} \in H$, where $H = H^m(\mathbb{T}^2)$ (see (2.1)) for some $m > 1$, with coefficients $c_{\mathbf{k}}$ given by (2.2).*

Here the exponent m is chosen so that vector fields in H , as well as their corresponding solutions $\theta(\mathbf{v})$, exhibit continuity properties convenient for our analysis below (see Proposition 2.2). We take $L^p(\mathbb{T}^2)$ with $p \in [1, \infty]$ for the usual Lebesgue spaces and denote the space of continuous and p -th integrable, X -valued functions by $C([0, T]; X)$ and $L^p([0, T]; X)$, respectively, for a given Banach space X . All of these spaces are endowed with their standard topologies unless otherwise specified.

In what follows we frequently consider Borel probability measures on H , denoted sometimes as $\Pr(H)$, in reference to the prior and posterior measures produced by Bayes' theorem below. A natural approach to construct certain classes of such infinite dimensional probability measures is to decompose them into one-dimensional probability measures acting independently on individual components of a sequence of elements sitting in an underlying function space; see e.g. [16, Section 2]. Concretely in our setting, probability measures on the space of divergence-free vector fields can be defined by letting $v_{\mathbf{k}}$ be random fields, as long as $v_{\mathbf{k}}$ exhibits suitable decay to zero as $\|\mathbf{k}\| \rightarrow \infty$ commensurate with $\mathbf{v} \in H$ (see Notation 2.1). In particular we make use of this construction on the space of divergence-free vector fields to define prior distributions in the numerical examples in Section 4.

2.2 Mathematical Setting for the Advection-Diffusion Equation

In this section, we provide a precise definition of solutions θ for the advection-diffusion problem (1.1). Crucially, the setting we choose yields a map from \mathbf{v} to θ and then to observations of θ that is continuous.

Proposition 2.2 (Well-Posedness and Continuity of the solution map for (1.1)).

- (i) Fix any $s \geq 0$ and $m \geq s$ with $m > 0$ and suppose that $\mathbf{v} \in H^m(\mathbb{T}^2)$ and $\theta_0 \in H^s(\mathbb{T}^2)$. Then there exists a unique $\theta = \theta(\mathbf{v}, \theta_0)$ such that

$$\theta \in L^2_{loc}([0, \infty); H^{s+1}(\mathbb{T}^2)) \cap L^\infty([0, \infty); H^s(\mathbb{T}^2)) \quad \text{with} \quad \frac{\partial \theta}{\partial t} \in L^2_{loc}([0, \infty); H^{s-1}(\mathbb{T}^2))$$

so that in particular $\theta \in C([0, \infty); H^s(\mathbb{T}^2))$ solves (1.1) at least weakly, namely

$$\left\langle \frac{\partial \theta}{\partial t}, \phi \right\rangle_{H^{-1}(\mathbb{T}^2) \times H^1(\mathbb{T}^2)} + \langle \mathbf{v} \cdot \nabla \theta, \phi \rangle_{L^2(\mathbb{T}^2)} + \kappa \langle \nabla \theta, \nabla \phi \rangle_{L^2(\mathbb{T}^2)} = 0 \quad (2.3)$$

for all $\phi \in H^1(\mathbb{T}^2)$ and almost all time $t \in [0, \infty)$.

- (ii) For any $T > 0$ the map that associates $\mathbf{v} \in H^m(\mathbb{T}^2)$ and $\theta_0 \in H^s(\mathbb{T}^2)$ to the corresponding $\theta(\mathbf{v}, \theta_0)$ is continuous relative the standard topologies on $H^m(\mathbb{T}^2) \times H^s(\mathbb{T}^2)$ and $C([0, T] \times H^s(\mathbb{T}^2))$.
- (iii) For any $T > 0, m \geq s > 1$ the map which associates $\mathbf{v} \in H^m(\mathbb{T}^2)$ and $\theta_0 \in H^s(\mathbb{T}^2)$ to the corresponding $\theta(\mathbf{v}, \theta_0)$ is continuous relative the standard topologies on $H^m(\mathbb{T}^2) \times H^s(\mathbb{T}^2)$ and $C([0, T] \times \mathbb{T}^2)$.

A sketch of the proof is provided in [9].

Remark 2.3. Since the background flow \mathbf{v} enters (1.1) through the $\mathbf{v} \cdot \nabla \theta$ term, the inverse problem of recovering \mathbf{v} from $\theta(\mathbf{v})$ can be ill-posed. One important class of examples illustrating this difficulty arises when $\mathbf{v} \cdot \nabla \theta$ is zero everywhere, in which case the fluid flow does not have any influence on θ . Two such examples are as follows:

- (i) Ill-posedness: Laminar Flow: Let $\theta_0(\mathbf{x})$ be independent of y and $\mathbf{v}^* = [0, f(x)]$. Then $\theta(\mathbf{v}^*) = \theta(\mathbf{v})$ for any $\mathbf{v} = [0, g(x)]$.
- (ii) Ill-posedness: Radial Symmetry: Set $\theta_0(\mathbf{x}) \propto \sin(\pi x) + \sin(\pi y)$ and $\mathbf{v}^* = [\cos(\pi x), -\cos(\pi y)]$. Then $\theta(\mathbf{v}^*) = \theta(\mathbf{v})$ for any $\mathbf{v} = c\mathbf{v}^*, c \in \mathbb{R}$.

In these cases, the even noiseless and complete spatial/temporal observations of θ cannot discriminate between a range of background flows, making it impossible to uniquely identify a true background flow \mathbf{v}^* .

With this general result in hand we now fix some notation used for the remainder of the paper.

Definition 2.4 (Solution Operator \mathcal{S} , Observation Operator \mathcal{O}). Fix $\theta_0 \in H^s(\mathbb{T}^2)$ and a final time $T > 0$ and consider the phase space H defined as in Notation 2.1. The forward map \mathcal{G} as in (1.2) is interpreted as the composition $\mathcal{G}(\mathbf{v}) = \mathcal{O} \circ \mathcal{S}(\mathbf{v})$, where:

1. The solution operator $\mathcal{S} : H \rightarrow C([0, T]; H^s(\mathbb{T}^2))$ maps a given \mathbf{v} to the corresponding solution $\theta(\mathbf{v}, \theta_0)$ of (1.1) (in the sense of Proposition 2.2).
2. The observation operator $\mathcal{O} : C([0, T]; H^s(\mathbb{T}^2)) \rightarrow Y$ measures some quantities (e.g. point measurements, spectral data, tracers) from θ . Here, in general, Y is a separable Hilbert space. However, since we are primarily focused on the setting of finite observations, we typically have $Y = \mathbb{R}^N$.

To make a connection with the range of observations provided in the introduction, we detail the following possibilities for \mathcal{O} .

Example 2.5. We consider finite observations $\mathcal{O}(\theta) = (\mathcal{O}_1(\theta), \dots, \mathcal{O}_N(\theta))$ that could be

1. Spectral Observations: $\mathcal{O}_j(\theta) = \int_{[0,1]^2} \theta(t_j, \mathbf{x}) e_j d\mathbf{x}$, with $\{e_j\}_{j \geq 0}$ an orthonormal basis for H^s and $t_j \in [0, T]$.

2. *Local averages:* $\mathcal{O}_j(\theta) = \frac{1}{|\mathcal{D}_j|} \int_{\mathcal{D}_j} \theta \, d\mathbf{x} \, dt$, for any sub-domains $\mathcal{D}_j \subset [0, T] \times [0, 1]^2$ where $|\mathcal{D}_j|$ denotes the volume of \mathcal{D}_j .
3. *Spatial-temporal point observations:* $\mathcal{O}_j(\theta) = \theta(t_j, \mathbf{x}_j)$ for any $t_j \in [0, T]$ and $\mathbf{x}_j \in [0, 1]^2$. (Note that point observations are well-defined by [Proposition 2.2](#), (iii).)

This paper focuses on final case of point observations $\mathcal{G}_j(\mathbf{v}) = \theta(t_j, \mathbf{x}_j, \mathbf{v})$, $j = 1, \dots, N$ as the most obvious practical implementation for the advection-diffusion problem.

2.3 Ill-posedness

We note that the classical inverse problem of recovering \mathbf{v} from data \mathcal{Y} (see [\(1.2\)](#)) is highly ill-posed in a number of ways:

1. The data is incomplete, i.e., we do not observe θ everywhere. For this reason we are interested in forward maps $\mathcal{G}(\mathbf{v})$ that are non-invertible and hence that do not uniquely specify \mathbf{v} . One such example is provided in [Section 4.2](#).
2. Even if solutions θ of [\(1.1\)](#) are observed everywhere in space and time, there are initial conditions θ_0 such that any of a range of background flows \mathbf{v} produce the same scalar field θ . Two such examples are provided in [Remark 2.3](#) above.
3. Because of the observational noise η in [\(1.2\)](#), there may be no \mathbf{v} such that $\mathcal{G}(\mathbf{v}) = \mathcal{Y}$ for given data \mathcal{Y} . For example, in the case of point observations $\mathcal{Y}_j = \theta(t_j, \mathbf{x}_j, \mathbf{v}^*) + \eta_j$, some realizations of η_j may cause \mathcal{Y}_j to exceed the maximum value (or be less than the minimum value) of θ_0 . However, because $\nabla \cdot \mathbf{v} = 0$, [\(1.1\)](#) is a parabolic PDE that is subject to a maximum principle implying $\|\theta(t)\|_{L^\infty(\mathbb{T}^2)} \leq \|\theta_0\|_{L^\infty(\mathbb{T}^2)}$ for all $t > 0$. Thus there would be no \mathbf{v} such that $\mathcal{G}(\mathbf{v}) = \mathcal{Y}$.

These considerations are typical of ill-posed inverse problems more broadly. See, e.g. [\[31, Section 2\]](#) or [\[49\]](#) for further commentary.

2.4 Bayesian Inference

Following the Bayesian approach to inverse problems [\[16, 31\]](#), instead of seeking a single best match \mathbf{v}^* , we take a statistical interpretation of \mathbf{v} and η as random quantities that we refer to as ‘the prior’ and ‘the observation noise’. The solution of [\(1.2\)](#) is a probability measure, known as the ‘posterior’, associated with the conditional random variable ‘ $\mathbf{v}|\mathcal{Y}$ ’. The concentration of the prior measure in the limit of a large number of observations, i.e. the question of consistency, is investigated in detail in [\[9\]](#). A quite general formulation of Bayes’ Theorem is provided in [Appendix C](#); in this section we follow closely the derivation in [\[16\]](#). We begin by imposing the following typical assumption:

Assumption 2.6. *The joint distribution of the observation noise and the prior take the form $(\mathbf{v}, \eta) \sim \mu_0 \otimes \gamma_0$ for $\mu_0 \in Pr(H)$, $\gamma_0 \in Pr(\mathbb{R}^N)$ so that \mathbf{v} and η are statistically independent.*

Under [Assumption 2.6](#), the ‘likelihood’ $\mathbb{Q}_{\mathbf{v}}$, heuristically $\mathcal{Y}|\mathbf{v}$, is

Lemma 2.7 (Likelihood $\mathbb{Q}_{\mathbf{v}}$). *For any deterministic background flow $\mathbf{v} \in H$ and observation noise $\eta \sim \gamma_0$, the likelihood $\mathbb{Q}_{\mathbf{v}}$ satisfies $\mathcal{G}(\mathbf{v}) + \eta \sim \mathbb{Q}_{\mathbf{v}}$ so that for any $A \in \mathcal{B}(\mathbb{R}^N)$,*

$$\mathbb{Q}_{\mathbf{v}}(A) = \gamma_0(\{y - \mathcal{G}(\mathbf{v}) : y \in A\}). \quad (2.4)$$

With the form of the likelihood measure $\mathbb{Q}_{\mathbf{v}}$ in hand we introduce the following notational convention used several times below

Notation 2.8 (True background flow, \mathbf{v}^*). *We frequently fix a “true” background flow by $\mathbf{v}^* \in H$. For the given \mathbf{v}^* , the observed data $\mathcal{Y} = \mathcal{G}(\mathbf{v}^*) + \eta$ can be viewed as draws from the distribution $\mathbb{Q}_{\mathbf{v}^*}$ (though \mathbf{v}^* is not necessarily the only \mathbf{v} that could produce such data).*

As in [\[16\]](#), we make the following assumption:

Assumption 2.9. *The likelihood $\mathbb{Q}_{\mathbf{v}}$ (see [Lemma 2.7](#)) is absolutely continuous with respect to the noise measure γ_0 for all $\mathbf{v} \in H$.*

We note that this assumption holds when γ_0 is any continuously distributed measure, such as a (non-degenerate) Gaussian, that has the whole space \mathbb{R}^N as its support. (We also note in [Proposition C.5](#) that γ_0 is not the only suitable choice of reference measure.) Then we define:

Definition 2.10 (Potential, Φ). *When [Assumption 2.9](#) holds, the potential or negative log-likelihood $\Phi : H \times \mathbb{R}^N \rightarrow \mathbb{R}$ is defined as*

$$\Phi(\mathbf{v}; \mathcal{Y}) = -\log \left(\frac{d\mathbb{Q}_{\mathbf{v}}}{d\gamma_0}(\mathcal{Y}) \right) \quad (2.5)$$

where $\frac{d\mathbb{Q}_{\mathbf{v}}}{d\gamma_0}$ is the Radon-Nikodym derivative of $\mathbb{Q}_{\mathbf{v}}$ with respect to γ_0 .

Example 2.11 (Gaussian Noise). *If the observation noise is a centered Gaussian, i.e. $\gamma_0 = N(0, \mathcal{C}_\eta)$, then by [\(2.4\)](#) we have (up to a factor independent of \mathbf{v})*

$$\Phi(\mathbf{v}; \mathcal{Y}) = \frac{1}{2} \left\| \mathcal{C}_\eta^{-1/2} (\mathcal{Y} - \mathcal{G}(\mathbf{v})) \right\|^2. \quad (2.6)$$

Finally, we have the following adaptation of Bayes' Theorem to the advection-diffusion problem:

Theorem 2.12 (Bayes' Theorem, [\[16\]](#)). *Let $\mathbb{Q}_{\mathbf{v}}$ and Φ be defined as in [Lemma 2.7](#) and [Definition 2.10](#), respectively, and let $\mathbb{Q}_{\mathbf{v}}$ satisfy [Assumption 2.9](#). Suppose that Φ is measurable in \mathbf{v} and \mathcal{Y} and that*

$$Z = \int \exp(-\Phi(\mathbf{v}; \mathcal{Y})) \mu_0(d\mathbf{v}) > 0. \quad (2.7)$$

Then the measure $\mu_{\mathcal{Y}}$ associated with the random variable $\mathbf{v}|\mathcal{Y}$ is absolutely continuous with respect to μ_0 , with Radon-Nikodym derivative

$$\frac{d\mu_{\mathcal{Y}}}{d\mu_0}(\mathbf{v}) = \frac{1}{Z} \exp(-\Phi(\mathbf{v}; \mathcal{Y})). \quad (2.8)$$

3 Computational Approach and Challenges

In this section, we describe the numerical methods used to approximate the posterior measure μ . We begin by introducing Markov Chain Monte Carlo (MCMC) methods used to generate samples from μ ([Section 3.1](#)). [Section 3.2](#) describes how we discretize and solve the advection-diffusion equation [\(1.1\)](#) to compute the potential Φ (see [Definition 2.10](#)). Finally, in [Section 3.3](#) we define an adjoint method for efficient computation of the Fréchet derivative $D\Phi$, which is required for implementation of some of the more advanced MCMC algorithms described in [Section 3.1](#).

3.1 Sampling from μ via Markov Chain Monte Carlo (MCMC)

To sample from the posterior measure $\mu_{\mathcal{Y}}$ (see [Theorem 2.12](#)), we use two Markov Chain Monte Carlo (MCMC) methods recently developed for or extended to infinite-dimensional problems: (1) preconditioned Crank-Nicolson (pCN) [\[14\]](#), a generalization of the classical random walk algorithm that requires one forward evaluation (PDE solve) per iteration and represents the “inexpensive” end of the computational spectrum (see [Algorithm 3.1](#)); and (2) Hamiltonian Monte Carlo (HMC) [\[11, 3, 17\]](#), a “computationally expensive” method that requires multiple PDE solves and gradient computations per iteration (see [Algorithm 3.2](#)). In [Appendix A](#), we additionally present some results for the independence sampler and Metropolis-adjusted Langevin Algorithm (MALA) (see, e.g., descriptions in [\[16\]](#) and [\[3\]](#), respectively). See also [\[38, Chapter 5\]](#) for a detailed description of these four methods and [\[30\]](#) for an algorithm to recursively select parameters for HMC.

Algorithm 3.1 Preconditioned Crank-Nicolson (pCN) MCMC.

-
- 1: Given free parameter $\beta \in (0, 1]$ and initial sample $\mathbf{v}^{(k)}$
 - 2: Propose $\tilde{\mathbf{v}} = \sqrt{1 - \beta^2} \mathbf{v}^{(k)} + \beta \xi^{(k)}$, $\xi^{(k)} \sim N(0, \mathcal{C})$
 - 3: Set $\mathbf{v}^{(k+1)} = \tilde{\mathbf{v}}$ with probability $\min\{1, \exp(\Phi(\mathbf{v}^{(k)}) - \Phi(\tilde{\mathbf{v}}))\}$, otherwise $\mathbf{v}^{(k+1)} = \mathbf{v}^{(k)}$
-

Algorithm 3.2 Hamiltonian MCMC (HMC).

-
- 1: Given free parameters $\tau \geq \epsilon > 0$ and initial sample $\mathbf{v}^{(k)}$. Set $L = \frac{\tau}{\epsilon}$.
 - 2: Set $(\mathbf{q}_0, \mathbf{w}_0) = (\mathbf{v}^{(k)}, \mathbf{w})$, where $\mathbf{w} \sim \mu_0 = N(0, \mathcal{C})$
 - 3: **for** $i = 1$ to L **do**
 - 4: Integrate Hamiltonian dynamics (compute Φ and $D\Phi$): $(\mathbf{q}_{i-1}, \mathbf{w}_{i-1}) \mapsto (\mathbf{q}_i, \mathbf{w}_i)$
 - 5: **end for**
 - 6: Compute $\Delta\mathcal{H} = \mathcal{H}(\mathbf{q}_L, \mathbf{w}_L) - \mathcal{H}(\mathbf{v}^{(k)}, \mathbf{w})$
 - 7: Set $\mathbf{v}^{(k+1)} = \mathbf{q}_L$ with probability $\min\{1, \exp[-\Delta\mathcal{H}]\}$, otherwise $\mathbf{v}^{(k+1)} = \mathbf{v}^{(k)}$
-

3.2 Evaluation of \mathcal{G}

Computing the potential $\Phi(\mathbf{v})$ (see [Definition 2.10](#)) as in [Algorithm 3.1](#) or [Algorithm 3.2](#) requires evaluating $\mathcal{G}(\mathbf{v})$, i.e., computing (e.g., point) observations for $\theta(\mathbf{v})$. This requires numerically solving (1.1) using a PDE solver. We do so using a spectral method [12, 23], expanding \mathbf{v} in a Fourier basis as in (2.1), (2.2) and θ similarly as $\theta(t, \mathbf{x}) = \sum_{\mathbf{k}} \theta_{\mathbf{k}}(t) e^{2\pi i \mathbf{k} \cdot \mathbf{x}}$. We apply a Galerkin projection, writing the coefficients $\theta_{\mathbf{k}}$ as a system of ODEs that reduces to

$$\frac{d}{dt} \vec{\theta}(t) = A \vec{\theta}(t), \quad \text{where } (A)_{lm} = -iv_{\mathbf{k}'} \left(\mathbf{k}'^\perp \cdot \mathbf{k}_m \right) - \kappa \|\mathbf{k}_l\|^2 \delta_{lm}, \quad \text{where } \mathbf{k}' = \mathbf{k}_l - \mathbf{k}_m. \quad (3.1)$$

This system is then integrated using the implicit midpoint (Crank-Nicolson) method to approximate $\vec{\theta}(t)$. Point observations are calculated as $\theta(t_j, \mathbf{x}_j) = \sum_{\mathbf{k}} \theta_{\mathbf{k}}(t_j) e^{2\pi i \mathbf{k} \cdot \mathbf{x}_j}$, with evaluation at time t_j interpolated if t_j does not fall on a timestep of the integration method. When κ is small, accurate representation of θ requires a large number of components due to the frequency cascade \mathbf{k}' in (3.1) (see [50]). This challenge motivates our concurrent work in [10], in which we introduce a particle method for efficient evaluation of $\mathcal{G}(\mathbf{v})$, allowing the computation of large numbers of samples for low- κ problems.

3.3 An Adjoint Method for Evaluating the Gradient of Φ

HMC ([Algorithm 3.2](#)) requires evaluating the Fréchet derivative of the potential Φ (see [Definition 2.10](#)) with respect to changes in \mathbf{v} , a direct approach to which would require many PDE solves. Here we introduce an adjoint approach that requires a single PDE solve per gradient computation using (a forced version of) the same solver used to solve (1.1). See also [29] for a detailed discussion of adjoint methods and [1], in which a similar adjoint equation was derived for a different application.

Theorem 3.1 (Adjoint Method for Evaluating $D\Phi$). *For a given background flow $\mathbf{v} \in H$, let $\theta(\mathbf{v}) \in H^m([0, T]; H^s(\mathbb{T}^2))$ be a weak solution of the advection-diffusion equation (1.1) in the sense that $\theta(0, \mathbf{x}) = \theta_0$ a.e. and*

$$\left\langle \rho, \frac{d}{dt} \theta + \mathbf{v} \cdot \nabla \theta - \kappa \Delta \theta \right\rangle_{H^{1-m, 2-s} \times H^{m-1, s-2}} = 0 \quad (3.2)$$

for all $\rho \in H^{1-m}([0, T]; H^{2-s}(\mathbb{T}^2))$. Suppose that Φ (see [Definition 2.10](#)) and $\mathcal{O} : H^m([0, T]; H^s(\mathbb{T}^2)) \rightarrow \mathbb{R}^N$ (see [Definition 2.4](#)) are continuously differentiable in \mathcal{G} and θ , respectively. Suppose there exists a $\rho_0 \in H^{1-m}([0, T]; H^{2-s}(\mathbb{T}^2))$ with $\rho_0(0, \mathbf{x}) = 0$ a.e. that solves the forced adjoint equation

$$\left\langle \frac{d}{dt} \rho_0 - \mathbf{v} \cdot \nabla \rho_0 - \kappa \Delta \rho_0, \phi \right\rangle_{H^{-m, -s} \times H^{m, s}} = - \frac{\partial \Phi}{\partial \mathcal{G}}(\mathbf{v}) \cdot \mathcal{O}[\tilde{\phi}] \quad (3.3)$$

for all $\phi \in H^m([0, T]; H^s(\mathbb{T}^2))$ with $\phi(T, \mathbf{x}) = 0$ a.e., where $\tilde{\phi}(t, \mathbf{x}) := \phi(T-t, \mathbf{x})$. Then the Fréchet derivative of Φ at \mathbf{v} in the direction $\hat{\mathbf{v}}$ is given by

$$D_{\hat{\mathbf{v}}} \Phi(\mathbf{v}) = \langle \tilde{\rho}_0, \hat{\mathbf{v}} \cdot \nabla \theta \rangle_{H^{1-m, 2-s} \times H^{m-1, s-2}} \quad (3.4)$$

where $\tilde{\rho}_0(t, \mathbf{x}) := \rho_0(T - t, \mathbf{x})$.

Proof. Application of the chain rule yields

$$D_{\hat{\mathbf{v}}}\Phi(\mathbf{v}) = \frac{\partial\Phi}{\partial\mathcal{G}}(\mathbf{v}) \cdot D_{\hat{\mathbf{v}}}\mathcal{G}(\mathbf{v}) = \frac{\partial\Phi}{\partial\mathcal{G}}(\mathbf{v}) \cdot \mathcal{O}[D_{\hat{\mathbf{v}}}\theta(\mathbf{v})]. \quad (3.5)$$

Denote $D_{\hat{\mathbf{v}}}\theta(\mathbf{v})$ by $\psi(\mathbf{v}, \hat{\mathbf{v}})$. Then by applying (3.2) to $\theta(\mathbf{v} + \epsilon\hat{\mathbf{v}})$ and $\theta(\mathbf{v})$, subtracting, taking the $\epsilon \rightarrow 0$ limit, and using the definition of the Fréchet derivative, we see that $\psi \in H^m([0, T]; H^s(\mathbb{T}^2))$ satisfies

$$\left\langle \rho, \frac{d}{dt}\psi + \mathbf{v} \cdot \nabla\psi - \kappa\Delta\psi + \hat{\mathbf{v}} \cdot \nabla\theta \right\rangle_{H^{1-m, 2-2s} \times H^{m-1, s-2}} = 0 \quad (3.6)$$

with $\psi(0, \mathbf{x}) = 0$ a.e., for all $\rho \in H^{1-m}([0, T]; H^{2-s}(\mathbb{T}^2))$. Also, changing variables from t to $T - t$ in (3.3) yields the following relationship for $\tilde{\rho}_0(t) = \rho_0(T - t)$:

$$\left\langle \frac{d}{dt}\tilde{\rho}_0 + \mathbf{v} \cdot \nabla\tilde{\rho}_0 + \kappa\Delta\tilde{\rho}_0, \tilde{\phi} \right\rangle_{H^{-m, -s} \times H^{m, s}} = \frac{\partial\Phi}{\partial\mathcal{G}}(\mathbf{v}) \cdot \mathcal{O}[\phi] \quad (3.7)$$

with $\tilde{\rho}_0(T, \mathbf{x}) = \tilde{\phi}(0, \mathbf{x}) = 0$ a.e. Then applying (3.5), (3.7), and (3.6) in succession yields

$$\begin{aligned} D_{\hat{\mathbf{v}}}\Phi(\mathbf{v}) &= \frac{\partial\Phi}{\partial\mathcal{G}}(\mathbf{v}) \cdot \mathcal{O}[\psi] = \left\langle \frac{d}{dt}\tilde{\rho}_0 + \mathbf{v} \cdot \nabla\tilde{\rho}_0 + \kappa\Delta\tilde{\rho}_0, \psi \right\rangle_{H^{-m, -s} \times H^{m, s}} \\ &= \left\langle \tilde{\rho}_0, -\frac{d}{dt}\psi - \mathbf{v} \cdot \nabla\psi + \kappa\Delta\psi \right\rangle_{H^{1-m, 2-2s} \times H^{m-1, s-2}} \\ &= \left\langle \tilde{\rho}_0, \hat{\mathbf{v}} \cdot \nabla\theta \right\rangle_{H^{1-m, 2-2s} \times H^{m-1, s-2}}, \end{aligned}$$

which is the desired result. \square

Remark 3.2. Note that $\left[\frac{\partial\Phi}{\partial\mathcal{G}}(\mathbf{v}) \cdot \mathcal{O}\right] \in H^{-m}([0, T]; H^{-s}(\mathbb{T}^2))$, so solving (3.3) amounts to finding the weak solution in $H^{-m}([0, T]; H^{-s}(\mathbb{T}^2))$ of

$$\frac{d}{dt}\rho_0 - \mathbf{v} \cdot \nabla\rho_0 - \kappa\Delta\rho_0 = \frac{\partial\Phi}{\partial\mathcal{G}}(\mathbf{v}) \cdot \tilde{\mathcal{O}}, \quad \rho_0(0, \mathbf{x}) = 0 \text{ a.e.}, \quad (3.8)$$

where $\tilde{\mathcal{O}}[\phi(t, \mathbf{x})] := \mathcal{O}[\phi(T - t, \mathbf{x})]$.

To compute the full gradient $D\Phi$ (the derivative with respect to an array of bases $\{\mathbf{e}_{\mathbf{k}}\}$), we compute the integration (3.4) for $\hat{\mathbf{v}} = \mathbf{e}_{\mathbf{k}}$ for each \mathbf{k} . The resulting algorithm is summarized in Algorithm 3.3. Note that solving (3.6) and substituting into (3.5) would also yield the derivative of Φ . However, this approach would require a PDE solve for each direction $\hat{\mathbf{v}}$ in which we want to take the derivative. In particular, if we want the full gradient, we have to do many PDE solves. By contrast, Algorithm 3.3 requires only one additional PDE solve per gradient calculation. Moreover, note that (3.8) is equivalent to (1.1) with zero initial condition, a reversed vector field, and a forcing term. Thus, the same PDE solver can be used for both the forward and adjoint solves with minimal modification. For the numerical experiments in Section 4, the adjoint equation (3.3) was solved using the same spectral method described in Section 3.2, where the forcing term was similarly expanded in the Fourier basis $e^{2\pi i \mathbf{k} \cdot \mathbf{x}}$ via Galerkin projection. The integration (3.4) was computed directly from the spectral representation of θ and ρ_0 , yielding

$$D_{\mathbf{e}_{\mathbf{k}}}\Phi(\mathbf{v}) = \sum_j 2\pi i (\mathbf{k}^\perp \cdot \mathbf{k}_j) \int_0^T \tilde{\rho}_{0_l}(t) \theta_j(t) \quad \text{where } l \ni \mathbf{k}_l = -\mathbf{k} - \mathbf{k}_j, \quad (3.9)$$

where the time integration was computed via trapezoidal rule.

Example 3.3 (Point Observations, Gaussian Noise). *Let the observation operator be point observations $\mathcal{O}_j[\theta] = \theta(t_j, \mathbf{x}_j)$. These observations are well-defined for $\theta \in H^m([0, T]; H^s(\mathbb{T}^2))$ with $m > \frac{1}{2}, s > 1$ (see Proposition 2.2, (iii)). Let $\eta_j \sim N(0, \sigma_\eta^2)$ for $j = 1, \dots, N$ so that Φ is given by (2.6). Then solving (3.3) amounts to finding the weak solution of*

$$\frac{\partial}{\partial t}\rho_0 - \mathbf{v} \cdot \nabla\rho_0 - \kappa\Delta\rho_0 = \sum_j \frac{1}{\sigma_\eta^2} (\mathcal{Y}_j - \theta(t_j, \mathbf{x}_j, \mathbf{v})) \delta(T - t_j - t, \mathbf{x} - \mathbf{x}_j),$$

where $\rho_0(0, \mathbf{x}) = 0$ a.e. and $\delta(t - t_0, \mathbf{x} - \mathbf{x}_0)$ is a Dirac distribution centered at (t_0, \mathbf{x}_0) .

Algorithm 3.3 Adjoint Method for Computing $D\Phi$.

-
- 1: Given \mathbf{v} and basis $\mathbf{e}_{\mathbf{k}}$
 - 2: Solve (1.1) for $\theta(t, \mathbf{x}, \mathbf{v})$
 - 3: Solve (3.3) for $\rho_0(t, \mathbf{x}, \mathbf{v})$
 - 4: **for** each \mathbf{k} **do**
 - 5: Compute $D_{\mathbf{k}}\Phi(\mathbf{v})$ via (3.4) with $\hat{\mathbf{v}} = \mathbf{e}_{\mathbf{k}}$
 - 6: **end for**
-

Example 3.4 (Integral Observations). *Let observations be given by $\mathcal{O}_j[\theta] = \langle f_j, \theta \rangle_{L^2([0, T] \times \mathbb{T}^2)}$ for some $f_j \in H^1([0, T]; H^2(\mathbb{T}^2))$. Let $\theta \in L^2([0, T]; L^2(\mathbb{T}^2))$ (i.e., $m = s = 0$ in Theorem 3.1). Let $\eta_j \sim N(0, \sigma_\eta^2)$ for $j = 1, \dots, N$ so that Φ is given by (2.6). Then solving (3.3) amounts to finding $\rho_0 \in H^1([0, T], H^2(\mathbb{T}^2))$ with $\rho_0(0, \mathbf{x}) = 0$ such that*

$$\frac{\partial}{\partial t} \rho_0 - \mathbf{v} \cdot \nabla \rho_0 - \kappa \Delta \rho_0 = \sum_j \frac{1}{\sigma_\eta^2} (\mathcal{Y}_j - \mathcal{O}_j[\theta(\mathbf{v})]) f_j(T - t, \mathbf{x}).$$

4 Numerical Experiments: Posterior Complexity and MCMC Convergence

In this section, we describe applications of the above methods to two sample problems. We begin with an example (Section 4.1) that yields a posterior measure with a relatively simple structure. This provides a baseline for measuring convergence of the pCN and HMC samplers (see Section 3.1), which for our purposes represent the “inexpensive” and “expensive” ends of the computational spectrum, respectively. Section 4.2 then presents a second example for which the posterior measure exhibits a complicated, multimodal structure. This example is more challenging for MCMC methods to sample from, and thus a good test of the advantages offered by more “expensive” methods like HMC. The appendices present analogous results for the IS and MALA samplers (Appendix A) and additional observables of interest to the passive scalar community (Appendix B).

In each example, we generate data \mathcal{Y} by running a high-resolution simulation of the system for a given true vector field \mathbf{v}^* and applying the observation operator \mathcal{O} . The PDE solver, adjoint solver, and MCMC methods were implemented in the Julia numerical computing language [8]. Thousands, or in some cases millions, of samples were generated using the computational resources at Virginia Tech.¹

4.1 Example 1: Single-welled Posterior

In this subsection, we construct an example that yields a posterior distribution with a simple, single-welled structure. The problem parameters for this example are enumerated in Table 1.² The true flow \mathbf{v}^* is shown in Figure 1.

Table 1: Problem parameters for Example 1.

Parameter	Value	Parameter	Value
Observation operator, \mathcal{O}	Point observations at 1,024 uniformly random (t, x, y)	Data, \mathcal{Y}	$\mathcal{G}(\mathbf{v}^*)$
Prior, μ_0	Kraichnan (4.2)	Noise, γ_0	$N(0, \sigma_\eta^2 I), \sigma_\eta = 2^{-6}$
True flow, \mathbf{v}^* (Figure 1)	Randomly drawn from Kraichnan prior, $\ \mathbf{k}\ _2 \leq 32$	Sampling space, H_N	$\ \mathbf{k}\ _2 \leq 8$ (197 components)
Diffusion, κ	0.282, for water in air [15]	θ_0	$\frac{1}{2} - \frac{1}{4} \cos(2\pi x) - \frac{1}{4} \cos(2\pi y)$

¹<http://www.arc.vt.edu>

²Note that \mathbf{v}^* and observation locations/times were chosen randomly only to generate the scenario and data. This random selection ensures a sufficiently general problem. The data and observation operator then of course remain fixed during MCMC sampling.

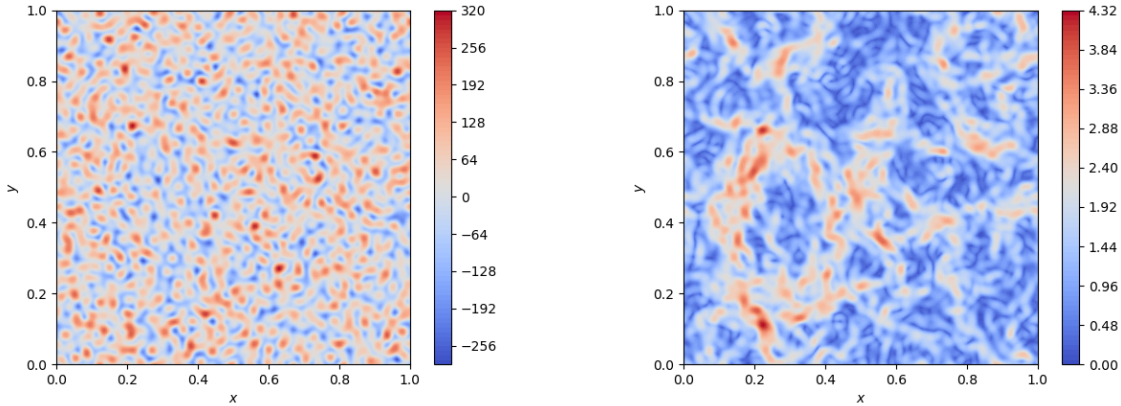


Figure 1: \mathbf{v}^* for Example 1. Left: Vorticity $\nabla \times \mathbf{v}^*$, Right: $\|\mathbf{v}^*\|$.

For the prior measure, we leverage the Kraichnan model [35, 36] of turbulent advection via a Gaussian random velocity field with energy spectrum (see [13, Equation 28])

$$E(k) = E_0 \sum_{i=0}^N \left(\frac{k}{k_i} \right)^4 \exp \left[-\frac{3}{2} \left(\frac{k}{k_i} \right)^2 \right] k_i^{-\xi} \quad (4.1)$$

where $k_i = \sqrt{2}^i$ is the characteristic wave number of the i th subfield, N is the number of subfields, and E_0 controls the overall energy. The resulting spectrum exhibits $E(k) \propto k^{-\xi}$ for $1 < k < k_N = 2^{N/2}$ and exponential decay for $k > k_N$. We then choose prior

$$\mu_0 = N(0, \tilde{E}), \quad \tilde{E}_{lm} = \frac{1}{2\pi \|\mathbf{k}_l\|_2} E(\|\mathbf{k}_l\|_2) \delta_{lm} \quad (4.2)$$

where E is as defined in (4.1), with $\xi = \frac{3}{2}$ motivated by [13, 37]. Then for $\mathbf{v} = \sum_{\mathbf{k}} v_{\mathbf{k}} \sim \mu_0$, the expected energy associated with wave numbers of norm k (integrating across the shell $S_k = \{\mathbf{k} : \|\mathbf{k}\|_2 = k\}$) is $E(k)$.

Note: The Kraichnan model of mixing typically involves a velocity field with energy spectrum (4.1) but that is white (δ -correlated) in time [47]. Here \mathbf{v} is a background flow, i.e. constant in time; we simply use the Kraichnan model as motivation for the energy decay modeled in the prior.

4.1.1 Posterior Structure

As described above, the output of a Bayesian inference is the posterior $\mu_{\mathcal{Y}}$, a probability measure on the space of divergence-free vector fields H or, in practice, on a finite-dimensional approximation H_N given by the truncated expansion of the basis described in Section 2.1. To approximate the exact posterior, we assembled a list of 10 million samples by running a series of 40 pCN MCMC chains of 250,000 samples each, with every chain beginning with an initial sample randomly chosen from the prior.³ Figure 2 shows the structure of the computed posterior. The left-hand plot shows mean, variance, skew, and excess kurtosis (kurtosis minus 3) of the posterior by Fourier component of \mathbf{v} , where \mathbf{v} , incorporating the discretization (2.1) and reality condition (2.2), is constructed from the components as:

$$\begin{aligned} \mathbf{v}(\mathbf{x}) = & [v_0, v_1] + v_2 [0, \cos(2\pi y)] + v_3 [0, -\sin(2\pi y)] + v_4 [\cos(2\pi x), 0] + v_5 [-\sin(2\pi x), 0] \\ & + v_6 [0, \cos(4\pi y)] + v_7 [0, -\sin(4\pi y)] + v_8 [\cos(2\pi x), \cos(2\pi y)] \\ & + v_9 [-\sin(2\pi x), -\sin(2\pi y)] + \dots \end{aligned} \quad (4.3)$$

³pCN was chosen here because it provided a computationally-inexpensive approximation to what proved to be a posterior with simple structure.

Because of the influence of the prior measure, the mean and covariance of the posterior for higher-order components tend to zero. Skew and excess kurtosis are near zero (up to computational resolution) for all components, indicating that the marginal distribution for each component is approximately Gaussian. The right-hand plot in [Figure 2](#) presents one- and two-dimensional histograms of the first eight components of \mathbf{v} . Note that the histograms (and other plots omitted for brevity) all show a contiguous mass of probability, indicating that one “class” of vector field matches both the prior and the data.

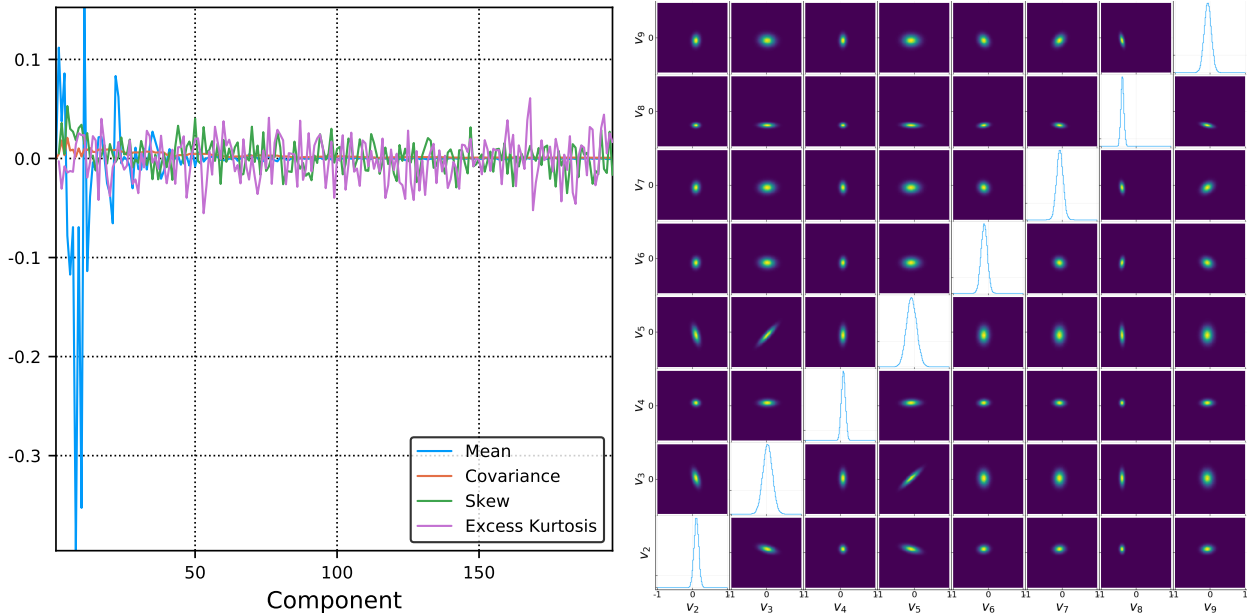


Figure 2: Structure of Posterior. Left: Mean, covariance, skew, and excess kurtosis of posterior measure, by component of \mathbf{v} . Right: Posterior ($\mu_{\mathcal{Y}}$) 1D (diagonal) and 2D (off-diagonal) marginal distributions for the first eight components of \mathbf{v} (out of 197).

4.1.2 MCMC Sampling

To test the behavior of “inexpensive” and “expensive” MCMC methods, both pCN and HMC (see [Section 3.1](#)) were applied to Example 1. The pCN parameter $\beta = 0.15$ was chosen to match the optimal acceptance rate of 23% from [\[45\]](#). For HMC, $\epsilon = 0.125$ and $\tau = 1$ were chosen because these values showed a good balance between the desire for high acceptance rate, large jumps between samples, and low computational cost in numerical experiments. The resulting acceptance rates were 23.9% for pCN and 81.0% for HMC. [Figure 3](#) shows the trace and autocorrelation of the potential Φ (see [Definition 2.10](#)). When pCN is applied to this example, we see “random walk” behavior – the samples move about the posterior, but are correlated with each other. For HMC, the random walk effect is reduced and samples exhibit independence from each other after orders of magnitude fewer iterations than for pCN. The HMC chain explores the posterior more quickly as a result. This is explored in the next section.

4.1.3 Convergence of Measures

The difference between the “true” ([Figure 2](#)) and computed marginal distributions can be evaluated via the total variation distance.⁴ Convergence of the MCMC chains to the true marginal distributions are shown in [Figure 4](#). The figure shows that HMC achieves a close approximation to the posterior marginal distributions within a few hundred iterations, while similar convergence takes about an order of magnitude longer for pCN.

⁴Note that the real desire would be to measure convergence in the full 197-dimensional sample space. In this paper, we will use the total variation norm to measure convergence between 1D and 2D distributions, a necessary and easy to picture – but not sufficient – requirement for convergence in the full-dimensional space.

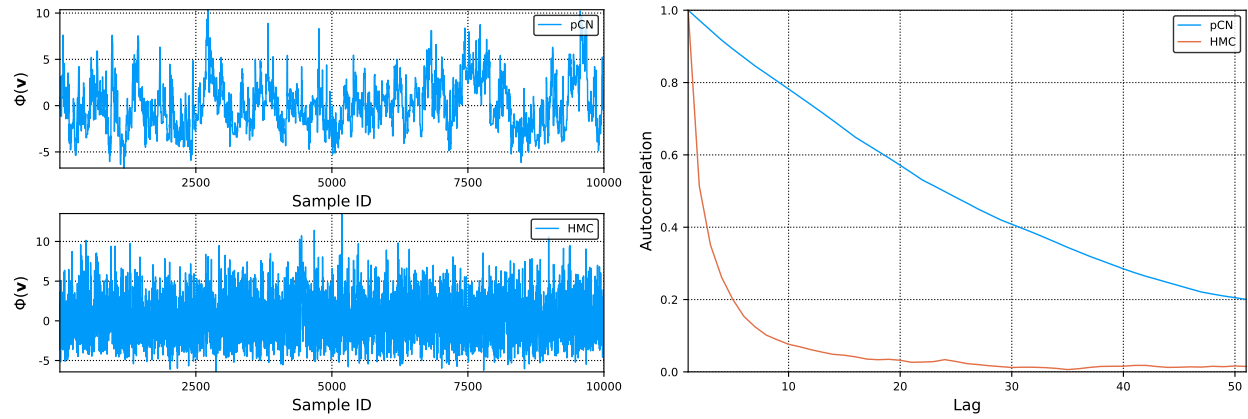


Figure 3: Trace (left) and autocorrelation (right) of the potential Φ .

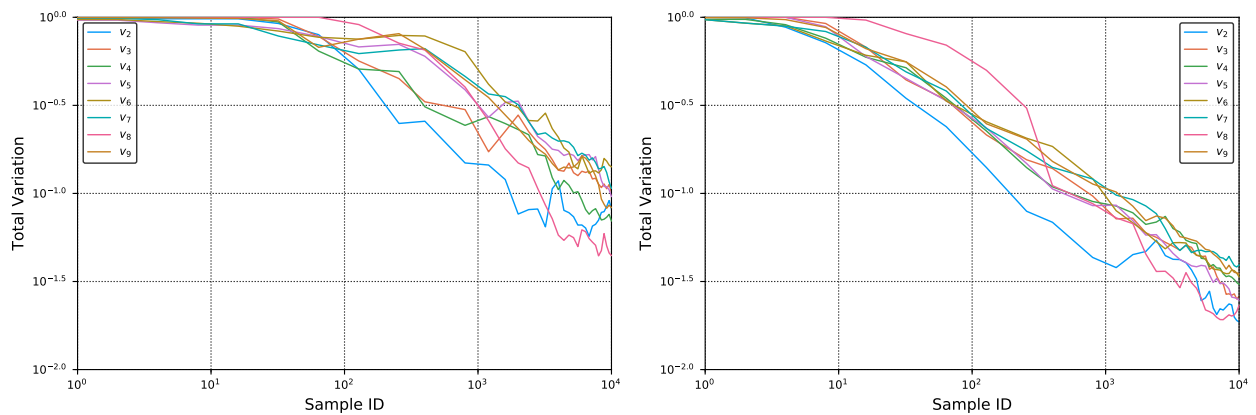


Figure 4: Total variation norm between computed and “true” marginal probability density function for v_2, \dots, v_9 for 10,000 samples. Left: pCN, Right: HMC.

4.1.4 Equal Runtime Comparison

Recall from Section 4.1.2 that the parameters used for HMC were $\epsilon = 0.125$ and $\tau = 1.0$, meaning that $\frac{\tau}{\epsilon} = 8$ PDE and adjoint solves (see Algorithm 3.2) were required per HMC sample. Because of these solves and the additional costs required for the gradient computation (see Algorithm 3.3) and time integration, each HMC sample took the time of approximately 39 pCN samples to compute. Thus, we can reweight pCN samples by 39 to get a comparison of the sampling accuracy per computational unit. Figure 5 shows the convergence of total variation norm for chains of runtime equal to 10,000 samples of HMC; the results can be compared with Figure 4. We see that chains of equal runtime are largely equivalent between the two methods when applied to Example 1; the faster convergence of HMC is essentially balanced by the larger amount of computation required to generate the samples.

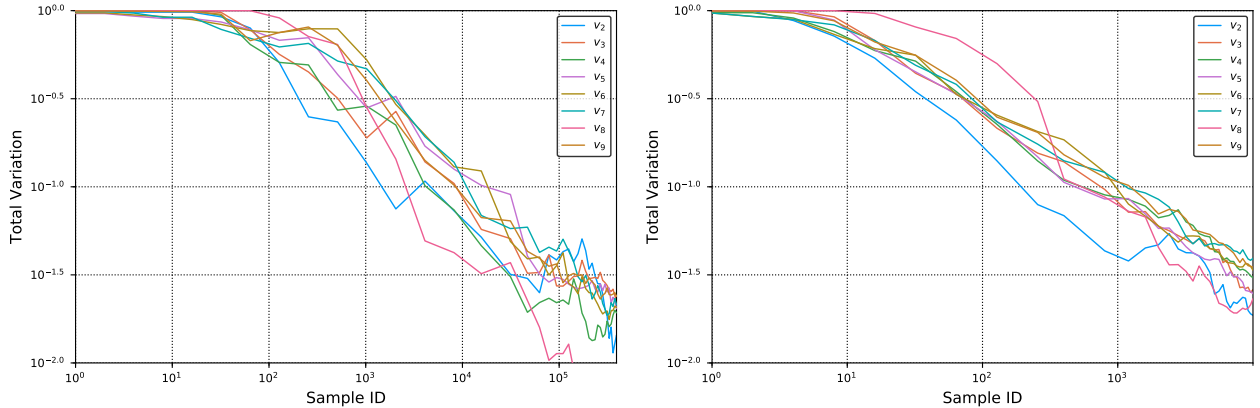


Figure 5: Total variation norm between computed and “true” marginal probability density function for v_2, \dots, v_9 for runtime equivalent to 10,000 HMC samples. Left: pCN, Right: HMC.

4.2 Example 2: Multimodal Posterior

In this section we present an example where the prior and data interact to produce a posterior with multiple regions of mass; posteriors of this kind are difficult for MCMC methods to resolve because chains have trouble jumping between the wells. We take the initial condition $\theta_0(\mathbf{x}) = \frac{1}{2} - \frac{1}{4} \cos 2\pi x - \frac{1}{4} \cos 2\pi y$ and true background flow $\mathbf{v}^* = [8 \cos 2\pi y, 8 \cos 2\pi x]$. Symmetry guarantees that for $\mathbf{x}_1 = [0, 0]$ and $\mathbf{x}_2 = [\frac{1}{2}, \frac{1}{2}]$ we have $\theta(\mathbf{v}^*, t, \mathbf{x}_i) = \theta(-\mathbf{v}^*, t, \mathbf{x}_i), i = 1, 2$. (In fact, there are more points for which this is true; however, two points suffice for the purposes of this example.) We therefore let the data \mathcal{Y} be point measurements $\theta(t, \mathbf{x})$ from $t = 0.001$ to 0.050 in intervals of 0.001 at each of \mathbf{x}_1 and \mathbf{x}_2 . Then we have $\Phi(\mathbf{v}^*) = \Phi(-\mathbf{v}^*)$, i.e. both \mathbf{v}^* and $-\mathbf{v}^*$ match the data equally well. Finally, we use the mean-zero Kraichnan prior (4.2), which assigns the same probability to both \mathbf{v}^* and $-\mathbf{v}^*$. The problem parameters for this example are listed in Table 2.

Since both \mathbf{v}^* and $-\mathbf{v}^*$ are given the same probability by both the prior and the data, they will be equally likely according to the posterior. We show in the next section that the symmetry in the problem setup results in multiple distinct probability masses in the posterior.

Table 2: Problem parameters for Example 2.

Parameter	Value	Parameter	Value
Observation operator, \mathcal{O}	Point observations at $\mathbf{x}_1 = [0, 0]$ and $\mathbf{x}_2 = [\frac{1}{2}, \frac{1}{2}]$	Data, \mathcal{Y}	$\mathcal{G}(\mathbf{v}^*)$
Prior, μ_0	Kraichnan (4.2)	Noise, γ_0	$N(0, \sigma_\eta^2 I), \sigma_\eta = 2^{-3}$
True flow, \mathbf{v}^*	$[8 \cos 2\pi y, 8 \cos 2\pi x]$	Sampling space, H_N	$\ \mathbf{k}\ _2 \leq 8$ (197 components)
Diffusion, κ	3×10^{-5} [13, Table I]	θ_0	$\frac{1}{2} - \frac{1}{4} \cos(2\pi x) - \frac{1}{4} \cos(2\pi y)$

4.2.1 Posterior Structure

As in Example 1, we approximate the exact posterior via a large number of samples; in this case we use 500,000 samples generated from 100 HMC chains of 5,000 samples apiece, each beginning with an initial sample randomly chosen from the prior measure. We chose HMC chains because they provided better convergence to the posterior than the other methods, as we describe below. Figure 6 shows the resulting posterior structure. The left plot shows the computed mean, variance, skew, and excess kurtosis of the posterior, by Fourier component of \mathbf{v} . We note that, due to the influence of the prior measure, the mean and covariance of the posterior tend to zero for higher-order components. Also, the deviations of excess kurtosis from zero indicate the presence of highly non-Gaussian marginal distributions for some components. The plot on the right presents one- and two-dimensional histograms for the first few components of \mathbf{v} (see the expansion in (4.3) for interpretation of the components). Note that the symmetry of the problem results in multiple large modes both v_2 and v_4 , as well as in several smaller bumps in the distributions of the other components.

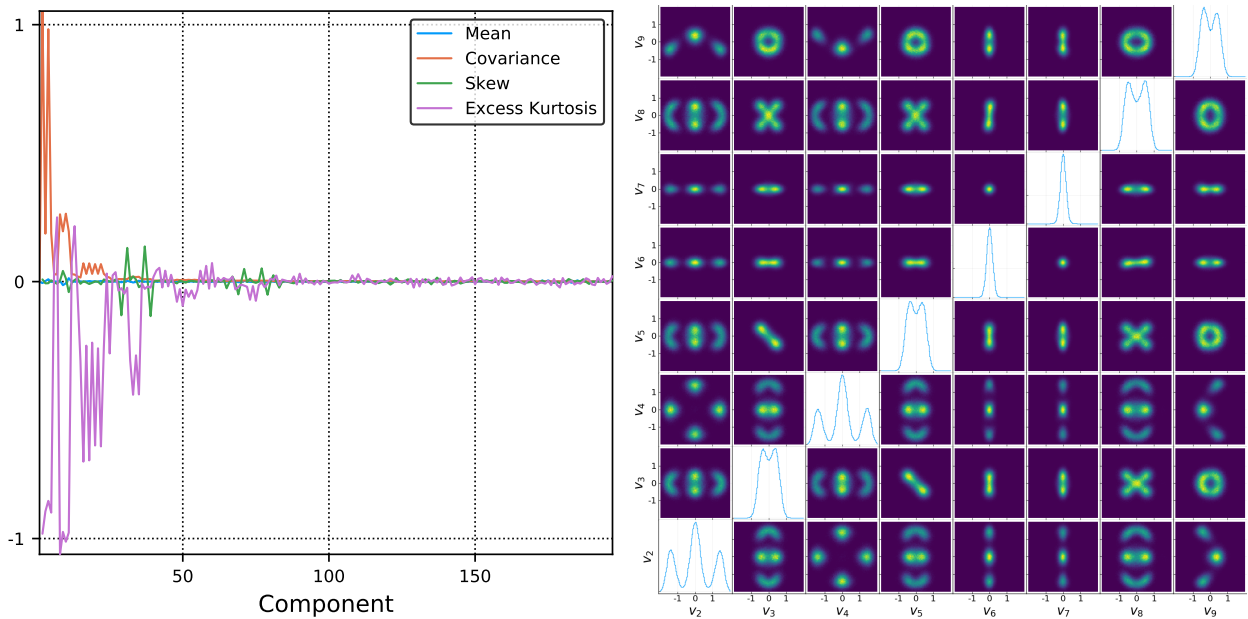


Figure 6: Structure of Posterior. Left: Mean, covariance, skew, and excess kurtosis of posterior measure, by component of \mathbf{v} . Right: Posterior ($\mu_{\mathcal{Y}}$) 1D (diagonal) and 2D (off-diagonal) marginal distributions for the first eight components of \mathbf{v} (out of 197).

Moreover, in contrast to Example 1, the two-dimensional histograms – the approximate posterior joint probability density of pairs of vector field components – show that the vector field components are highly correlated with each other (see, e.g., the “X” shape between v_3 and v_8). It is worth noting that the posterior contains these correlation structures even though the prior assumes independence of the components.

Finally, it is worth noting that not all observables of the posterior exhibit complicated structures. Figure 7 shows the computed posterior one- and two-dimensional histograms of background flow vorticity at nine observation locations. The one-dimensional histograms are simple – i.e., nearly Gaussian – at each point. However, the two-dimensional histograms (except at the center point, \mathbf{x}_5), exhibit multiple modes of different shapes.

4.2.2 MCMC Sampling

The multimodal structure of the posterior is typical of distributions that are difficult for MCMC methods to resolve efficiently, as the chains have difficulty moving across the regions of low probability between the regions of mass. We now use this structure to test the viability of pCN and HMC (see Section 3.1) in resolving complicated posteriors. The tests use parameter values of $\beta = 0.2$ for pCN (again corresponding

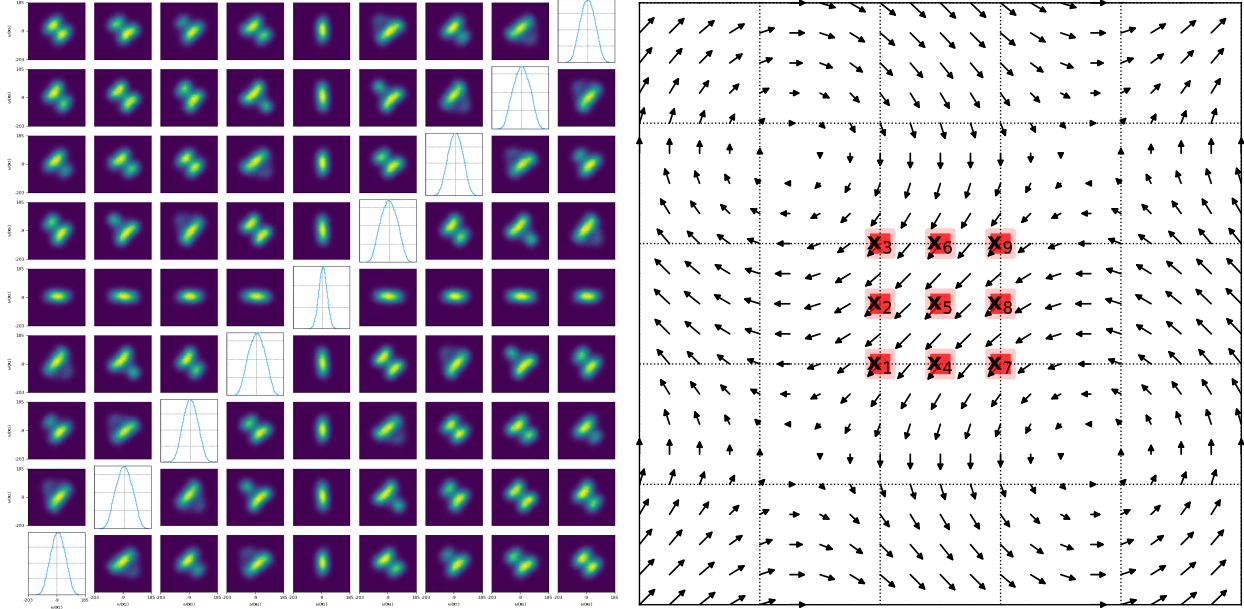


Figure 7: Posterior one- and two-dimensional histograms of vorticity (left) at nine observation points (shown against \mathbf{v}^* , right).

to the optimal acceptance rate of 23% from [45]) and $\epsilon = 0.125$ and $\tau = 4$ for HMC, which in numerical experiments showed good convergence behavior.

Figure 8 shows the trace and autocorrelation of the potential Φ (see Definition 2.10) for MCMC sampling of Example 2. As in Example 1, we see “random walk” behavior for pCN, whereas for HMC many fewer iterations are required to achieve statistical independence between samples. Unlike Example 1, however, the HMC chains for Example 2 exhibit negative autocorrelation between consecutive samples. The author plans to investigate this phenomenon, which may be related to the multimodal structure of the problem, in later work.

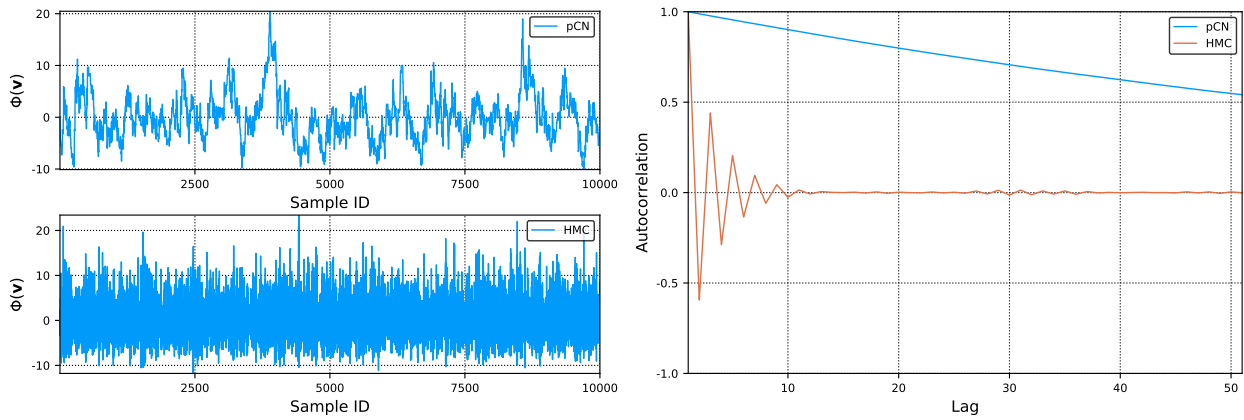


Figure 8: Trace (left) and autocorrelation (right) of the potential Φ .

We can also see the contrast between pCN and HMC in the traces of vector field components shown in Figure 9. The pCN samples move within a relatively limited range (a single probability mass), while the HMC samples occasionally jump between the different probability regions. In parameter testing, we observed that the frequency of these jumps increased roughly linearly with τ ($\tau = 4$ produced twice as many jumps as $\tau = 2$, for example) because longer integration times allowed the Hamiltonian system to evolve further,

overcoming the areas of low probability that separate the regions of mass.

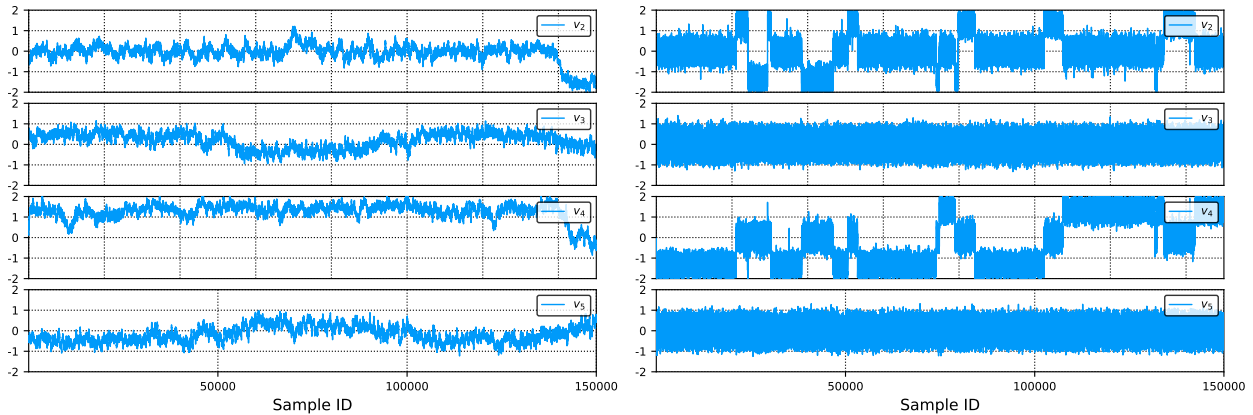


Figure 9: Trace of v_2, \dots, v_5 by sample number, pCN (left) and HMC (right).

4.2.3 Convergence of Measures

We now consider how the computed probability density functions (normalized histograms) compare for each of the MCMC methods. Figure 10 shows the computed one- and two-dimensional distributions for the first few vector field components after 150,000 samples. This figure can be compared with the “true” distributions shown in Figure 6. The histograms for pCN show only some of the many distinct probability regions in the posterior, as the chain failed to jump across the regions of low probability. The distributions for v_2 and v_4 , in particular, only show one or two of the three modes shown in Figure 6. The histograms for HMC, by contrast, resolve all major features in the posterior, though some of the features still exhibited imbalance when the chain terminated. The asymmetry in v_4 and v_9 indicates that the chain has perhaps not fully converged yet.

As in Example 1, we can get a feel for convergence of the methods by computing the total variation distance between the “true” μ and N -sample $\mu^{(N)}$ marginal distributions. The results are shown in Figure 11. We note the “sawtooth” behavior for HMC, as the number of samples in each mode of, for example, v_4 slowly balances.

4.2.4 Equal Runtime Comparison

It is worth noting that, due to the selected values of the parameters ϵ and τ , the HMC method used above required 32 PDE and 32 adjoint solves per sample, making it quite expensive relative to a sample of pCN. In our implementation, we were able to compute 125 pCN samples for each HMC sample. As a result, almost 19 million pCN samples could be computed in the time required to generate 150,000 HMC samples. For comparison in terms of equal computational cost, we now present the results of a single 19 million-sample pCN chain with the 150,000 sample HMC run shown earlier. Figure 12 compares the trace of the first few vector field components by sample number. We see that pCN does eventually achieve the jumps between states that HMC shows; however, the jumps are much less frequent for pCN, even when weighted by runtime, than for HMC (approximately 5 jumps vs. 20 jumps, respectively).

Figure 13 shows the computed one- and two-dimensional histograms for the 19 million-sample pCN chain, which can be compared with the HMC figure in Figure 10. Figure 14 compares the evolution of the total variation norm between the computed and “true” two-dimensional distributions for pCN (blue) and HMC (orange) chains of equal runtime. (Convergence of the (v_2, v_9) correlation structure, for example, is shown in the bottom right subplot.) These two plots are more equivocal between the two methods. pCN produces better convergence for histograms with one probability mode (e.g., the pair (v_6, v_7)); for these components, the extra computations involved in HMC (which was tuned for larger jumps) do not appear to provide a benefit. However, the two methods exhibited very similar convergence for multimodal distributions (e.g., those associated with v_2 or v_4). HMC also reached all of the modes in the distribution, while pCN generated

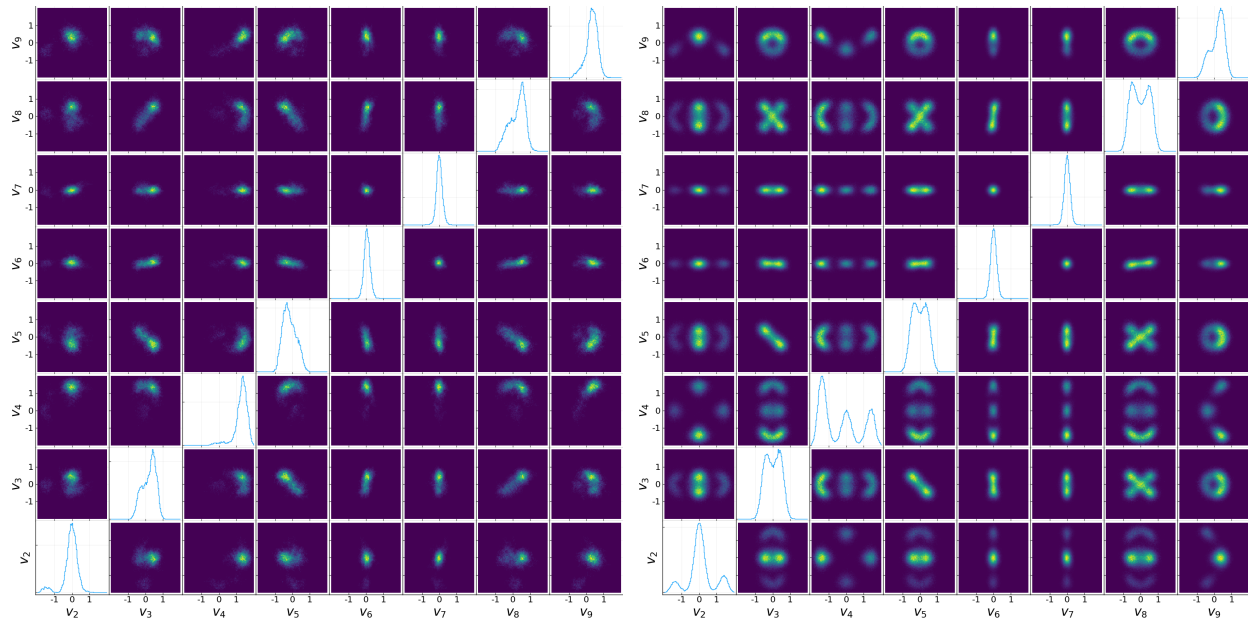


Figure 10: Computed 1D and 2D marginal distributions for each of the first eight vector field components (out of 197) for 150,000 samples, pCN (left) and HMC (right).

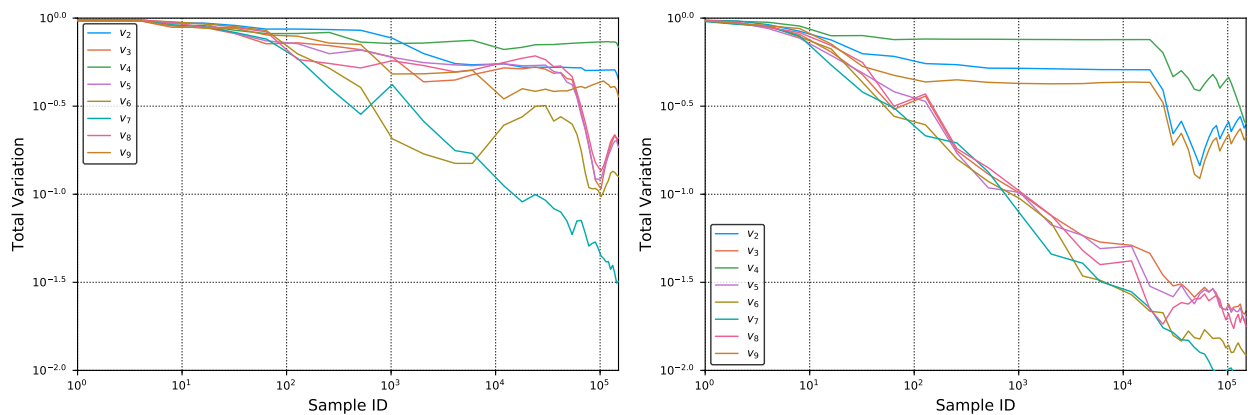


Figure 11: Total variation norm between computed (150,000 samples) and “true” marginal probability density function for v_2, \dots, v_9 , pCN (left) and HMC (right).

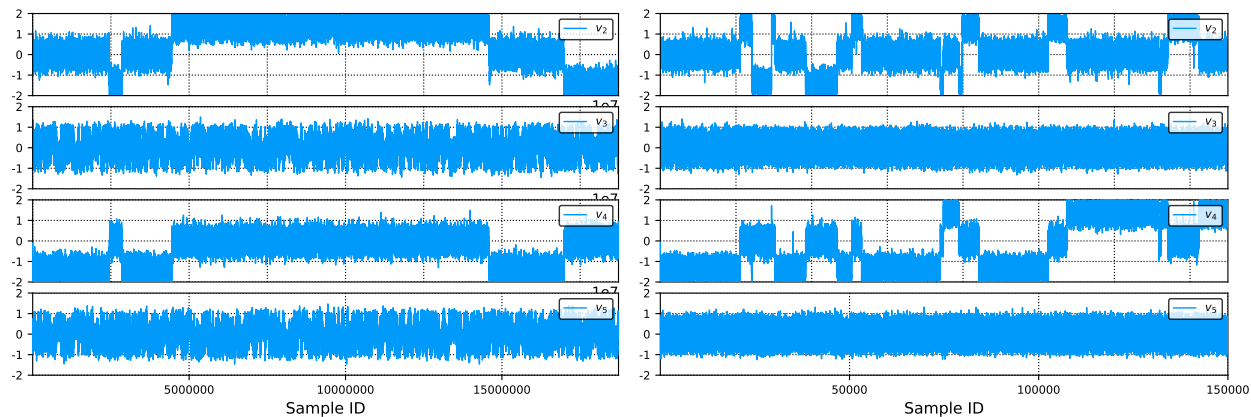


Figure 12: Trace of v_2, \dots, v_5 by sample number for runtime equivalent to 150,000 HMC samples, pCN (left) and HMC (right).

no samples in the mode near $v_4 \approx 1.5$. Overall, it appears that pCN did a better job (on an equal-runtime basis) of sampling within modes while HMC did a better job of finding modes.

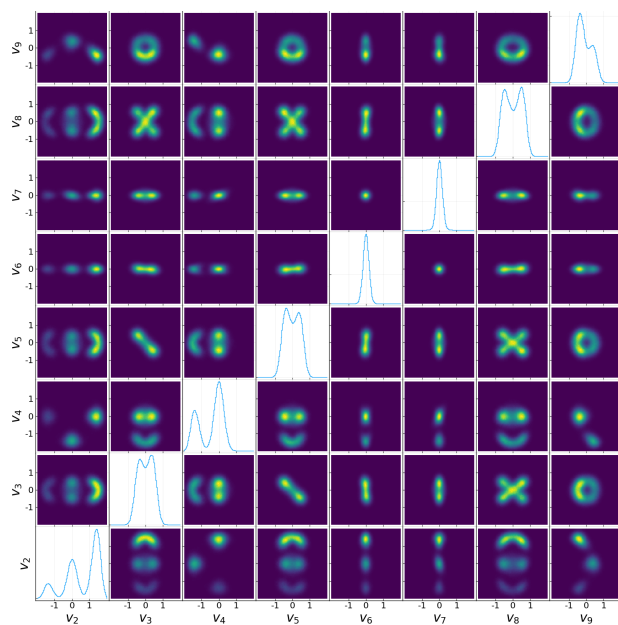


Figure 13: Computed 1D and 2D marginal distributions for each of the first eight vector field components (out of 197) for 19 million samples of pCN (same runtime as 150,000 samples of HMC).

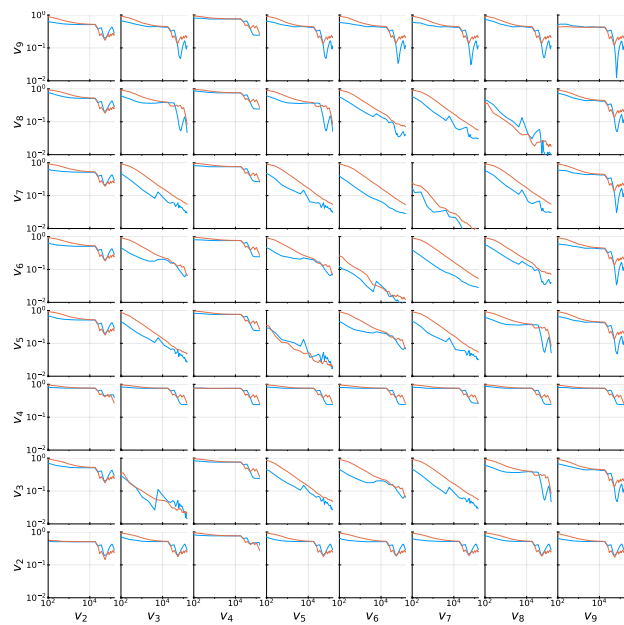


Figure 14: Total variation norm between computed and “true” 2D probability density for pairs of vector field components for pCN (blue) and HMC (orange) of equal computational time.

4.3 Summary of Numerical Experiments

To summarize the results of Examples 1 and 2, we see trade-offs between the MCMC methods:

- pCN provides an inexpensive method to generate samples and explore local regions of a probability measure, with a free parameter β that can be tuned to the problem.

- HMC samples are more computationally expensive to generate; for the HMC test cases reported here, each HMC sample took 39-125 times as much time as one pCN sample, though in general this ratio will be dictated by the cost of the gradient computation and the choice of number of integration steps $\frac{\tau}{\epsilon}$.
- In our numerical experiments, for posterior distributions with simple structure (e.g., Example 1 or some parts of Example 2), pCN exhibits similar (as measured by equal number of samples) or better (as measured by equal runtime) convergence to HMC.
- In our numerical experiments, for posterior distributions with more complicated structure (some components in Example 2), pCN still appeared to do a better job (for equal runtime) of sampling within probability modes, while HMC appeared to do a better job of jumping between states to find new modes. The overall impact on performance is difficult to discern and will likely depend heavily on the desired observables.
- Finally, we note that implementation of HMC is much more involved than pCN. With a working PDE solver, pCN can be implemented in a matter of minutes or hours. Developing a gradient solver and implementing the HMC leap frog integration (and debugging both) – if even possible – can require on the order of days or months of development time, depending on the complexity of the PDE solver.

A Selected Numerical Results for the IS and MALA Algorithms

In the main body of the paper, we present MCMC results for the preconditioned Crank-Nicolson (pCN, [Algorithm 3.1](#)) and Hamiltonian (HMC, [Algorithm 3.2](#)) MCMC algorithms. Here we also present results for the independence sampler (IS) and Metropolis-adjusted Langevin (MALA) methods. IS, a special case of pCN when μ_0 is Gaussian, draws proposals from the prior and requires one PDE solve per iteration. MALA uses one PDE and adjoint solve per iteration and is therefore more computationally expensive than iterations of IS or pCN but in general less computationally expensive than those of HMC.

Algorithm A.1 Independence Sampler MCMC.

- 1: Given sample $\mathbf{v}^{(k)}$
 - 2: Propose $\tilde{\mathbf{v}} \sim \mu_0$
 - 3: Set $\mathbf{v}^{(k+1)} = \tilde{\mathbf{v}}$ with probability $\min\{1, \exp(\Phi(\mathbf{v}^{(k)}) - \Phi(\tilde{\mathbf{v}}))\}$, otherwise $\mathbf{v}^{(k+1)} = \mathbf{v}^{(k)}$
-

Algorithm A.2 Metropolis-Adjusted Langevin (MALA) MCMC.

- 1: Given free parameter h and sample $\mathbf{v}^{(k)}$
- 2: Propose $\tilde{\mathbf{v}} = \frac{2-h}{2+h}\mathbf{v}^{(k)} - \frac{2h}{2+h}\mathcal{C}D\Phi(\mathbf{v}^{(k)}) + \frac{\sqrt{8h}}{2+h}\xi^{(k)}$, $\xi^{(k)} \sim N(0, \mathcal{C})$
- 3: Set $\mathbf{v}^{(k+1)} = \tilde{\mathbf{v}}$ with probability $\alpha(\mathbf{v}^{(k)}, \tilde{\mathbf{v}}) = 1 \wedge \exp(\rho(\mathbf{v}^{(k)}, \tilde{\mathbf{v}}) - \rho(\tilde{\mathbf{v}}, \mathbf{v}^{(k)}))$, where $\rho(\mathbf{v}, \tilde{\mathbf{v}})$ is given by

$$\rho(\mathbf{v}, \tilde{\mathbf{v}}) = \Phi(\mathbf{v}) + \frac{1}{2}\langle \tilde{\mathbf{v}} - \mathbf{v}, D\Phi(\mathbf{v}) \rangle + \frac{h}{4}\langle \mathbf{v} + \tilde{\mathbf{v}}, D\Phi(\mathbf{v}) \rangle + \frac{h}{4}\left\|\mathcal{C}^{\frac{1}{2}}D\Phi(\mathbf{v})\right\|^2 \quad (\text{A.1})$$

Otherwise $\mathbf{v}^{(k+1)} = \mathbf{v}^{(k)}$ (unchanged)

A.1 Example 1

Here we present IS and MALA results for numerical Example 1 (see [Section 4.1](#)). For MALA, we chose $h = 0.005$ to approximate the optimal acceptance rate of 57% from [\[45\]](#). The actual acceptance rates for IS and MALA were 0.012% and 53.7%, respectively. The chain concluded with thousands of consecutive rejections. [Figure 15](#), an extension of [Figure 15](#) to four methods, shows convergence, as measured by total variation norm, of the 1D marginal distributions to the “true” marginal distributions shown in the diagonal of [Figure 2](#). We observe IS failing to converge due to the high number of rejections. MALA converges at roughly the same rate as pCN.

[Figure 16](#), an extension of [Figure 5](#) to four methods, shows the same total variation convergence normalized by runtime. IS samples are roughly the same cost to generate as pCN samples, so 39 IS samples were generated per HMC sample. Similarly, an HMC sample took roughly 8 times as long to generate as a MALA sample because the version of HMC used in Example 1 required eight PDE and adjoint solves per sample, while MALA only requires one of each. Thus, we can reweight IS and pCN samples by 39 and MALA samples by 8 to get a comparison of the sampling accuracy per unit time. IS again fails to exhibit any meaningful convergence. MALA converges somewhat slower than either pCN or HMC, the former because MALA samples took more than twice as long to generate due to the need for an adjoint solve at each iteration.

A.2 Example 2

For Example 2 (see [Section 4.2](#)), we chose $h = 0.001$ for MALA to again match the optimal acceptance rate from [\[45\]](#). [Figure 17](#), which can be compared with analogous plots for pCN and HMC in [Figure 10](#), shows the computed 1D and 2D histograms for each of the first eight vector field components (out of 197) for 100,000 MALA samples. We see that the MALA chain failed to resolve the multiple modes of the posterior measure seen in [Figure 6](#).

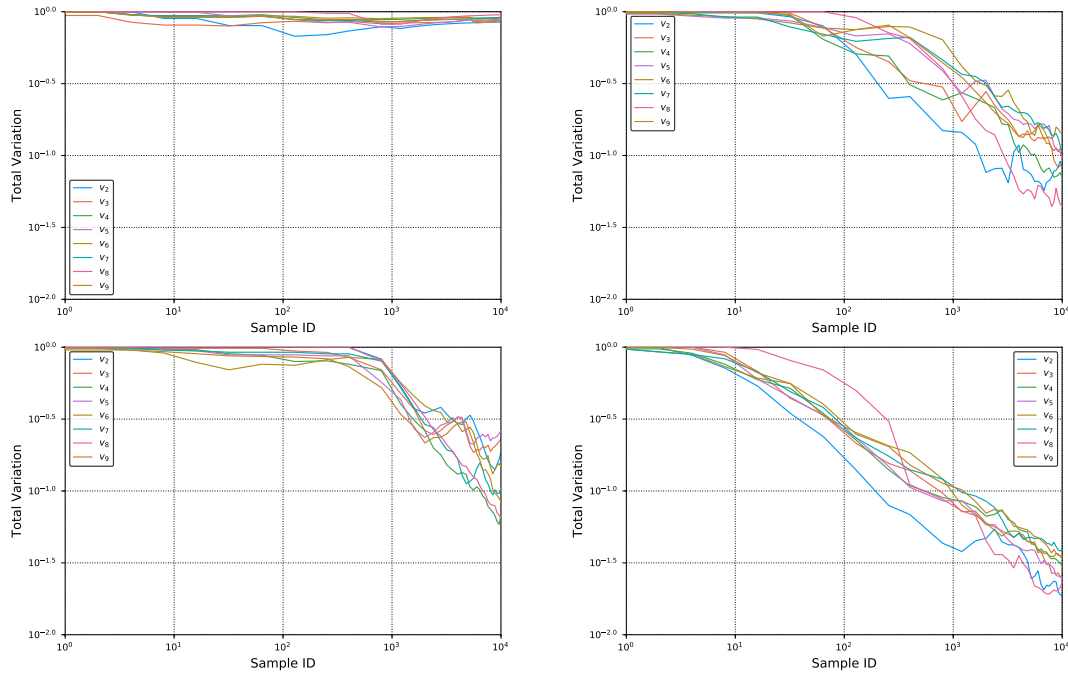


Figure 15: Total variation norm between computed and “true” marginal probability density function for v_2, \dots, v_9 for 10,000 samples, Example 1. Top Left: IS, Top Right: pCN, Bottom Left: MALA, Bottom Right: HMC.

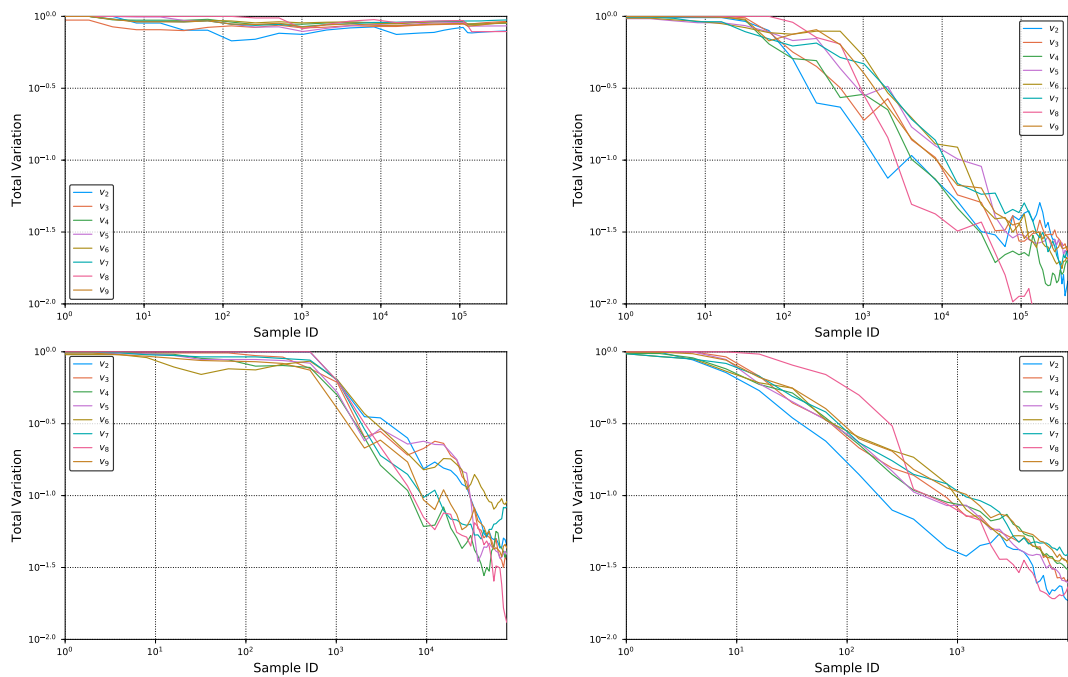


Figure 16: Total variation norm between computed and “true” marginal probability density function for v_2, \dots, v_9 for runtime equivalent to 10,000 HMC samples, Example 1. Top Left: IS, Top Right: pCN, Bottom Left: MALA, Bottom Right: HMC.

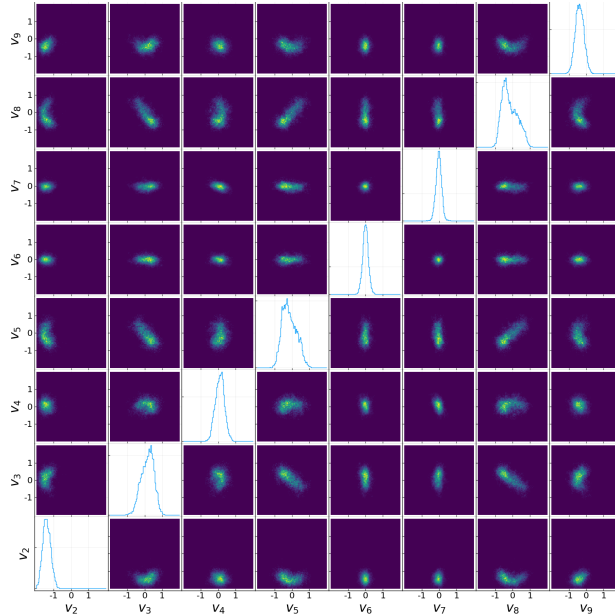


Figure 17: Computed 1D and 2D marginal distributions for each of the first eight vector field components (out of 197) for 100,000 samples of MALA, Example 2. (Compare with Figure 10.)

B Convergence of Observables

In this section, we compare pCN and HMC convergence for a series of observables that are of interest to the passive scalar community. These observables, which involve both \mathbf{v} and θ , are summarized in Table 3. Convergence is measured as relative error of the mean vs. the mean given by the computed “true” posterior measures shown in Figure 2 for Example 1 and Figure 6 for Example 2.

Table 3: Observables.

Observable	Formula
Mean Scalar Variance [54]	$\ \theta - \bar{\theta}\ _{L^2}^2$
Mean Scalar Dissipation Rate [47, 54]	$\epsilon_\theta = 2\kappa \ \nabla\theta\ _{L^2}^2$
Enstrophy [39, 2]	$\frac{1}{2}\ \nabla \times \mathbf{v}\ _{L^2}^2$
Enstrophy Dissipation Rate	$\ \nabla(\nabla \times \mathbf{v})\ _{L^2}^2$
Scalar Differences [47, 54]	$\Delta_r\theta = \theta(\mathbf{x} + \mathbf{r}, t) - \theta(\mathbf{x}, t)$

B.1 Example 1

In this section, we compare convergence of observables for the single-mode posterior in Example 1 (see Section 4.1). Figure 18 shows the relative error in the mean value of the first four observables in Table 3 at $t = 1$, through 10,000 samples.⁵ HMC converges an order of magnitude more quickly than pCN.

More challenging observables to resolve are scalar differences (see Table 3), which require resolving θ at two different locations. Figure 19 shows convergence results for the mean values (cumulative moving averages) of scalar differences with $\mathbf{x} = [0, 0]$ and $\mathbf{r}_i = 2^{-i}[1, 1]$ for $i = 1, 2, 3, 4$, up to 100,000 samples (10 times longer than the results shown in Figure 18). Convergence for scalar differences is much slower than for

⁵The sharp downward dips in these relative error plots occur when a cumulative moving average drifts past the “true” value. At these points, the relative error is zero, so a log plot exhibits a downward dip toward $\log(0) = -\infty$.

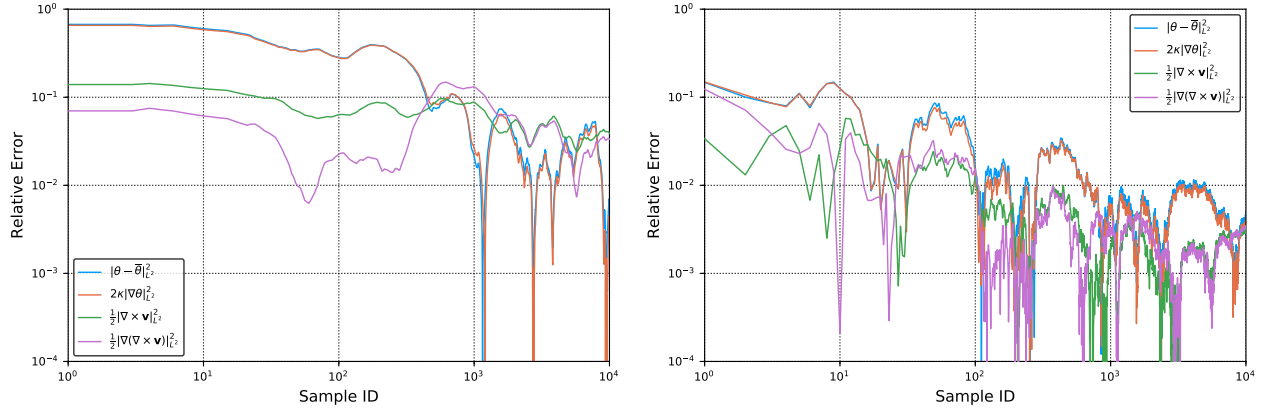


Figure 18: Relative error for the mean (cumulative moving average) of observables scalar variance, scalar dissipation rate, enstrophy, and enstrophy dissipation for 10,000 samples, Example 1. Left: pCN, Right: HMC.

the observables in Figure 18, though again we see that the relative error decays more quickly for HMC than for pCN. For both methods, the convergence is fairly uniform across scales – the various scalar differences converge at the same rates.

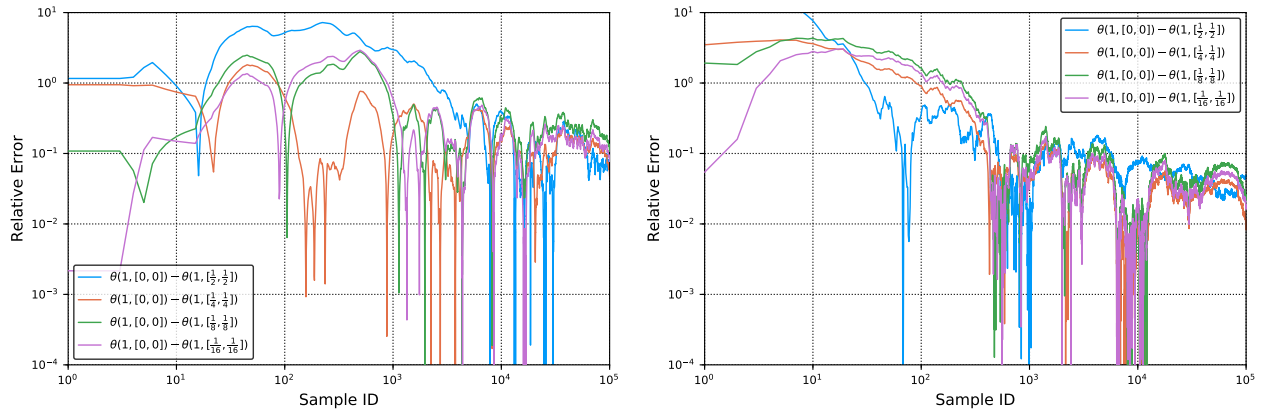


Figure 19: Relative error for the mean (cumulative moving average) of scalar differences at $t = 1$ between the origin and $[\frac{1}{2}, \frac{1}{2}]$, $[\frac{1}{4}, \frac{1}{4}]$, $[\frac{1}{8}, \frac{1}{8}]$, $[\frac{1}{16}, \frac{1}{16}]$ for 100,000 samples, Example 1. Left: pCN, Right: HMC.

B.2 Example 2

In this section, we compare convergence of observables for the multimodal problem in Example 2 (see Section 4.2). Figure 20 shows the cumulative moving average of scalar variance, scalar dissipation rate, enstrophy, and enstrophy dissipation (see Table 3) for pCN and HMC. The means for both methods converge, though HMC converges in an order of magnitude fewer samples than pCN.

Figure 21 shows similar convergence plots for scalar differences (see Table 3), which proved much harder for the MCMC methods to resolve; the figure shows results through 150,000 samples (15 times more samples than in Figure 20). Scalar differences across small distances proved much more difficult for the methods to resolve than the longer distances; pCN, in particular, shows almost no convergence for the two shorter-range differences. The analogous plots for HMC begin to exhibit a sawtooth shape as the number of samples grows; this is the result of balancing between the number of samples that the chain produces in each of the various probability modes due to the jumps seen in Figure 9.

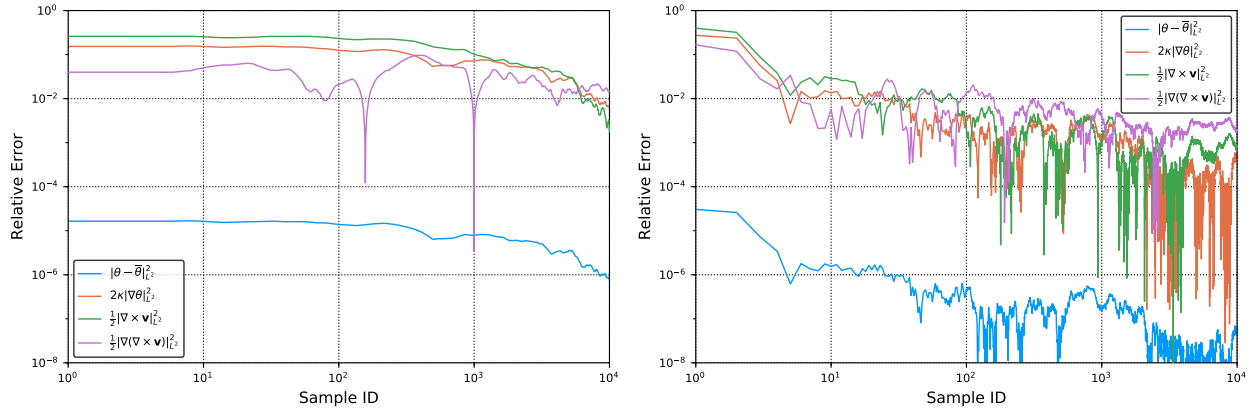


Figure 20: Relative error for the mean (cumulative moving average) of observables scalar variance, scalar dissipation rate, enstrophy, and enstrophy dissipation for 10,000 samples, Example 2. Left: pCN, Right: HMC.

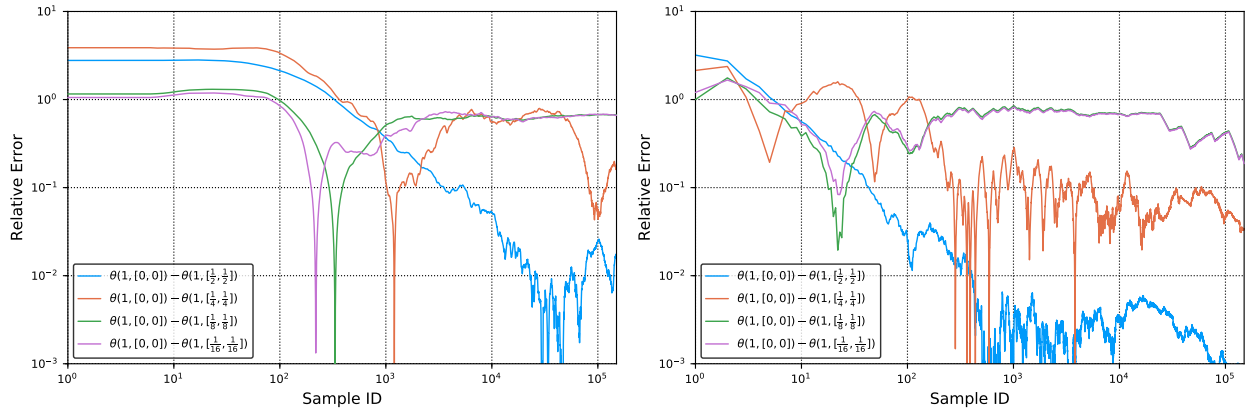


Figure 21: Relative error for the mean (cumulative moving average) of scalar differences at $t = 1$ between the origin and $[\frac{1}{2}, \frac{1}{2}]$, $[\frac{1}{4}, \frac{1}{4}]$, $[\frac{1}{8}, \frac{1}{8}]$, $[\frac{1}{16}, \frac{1}{16}]$ for 100,000 samples, Example 2. Left: pCN, Right: HMC.

C A General Setting for Bayes' Theorem

In this Appendix we consider an infinite dimensional setting for a Bayesian Theorem applicable to a broad class of statistical inverse problems that includes the problem considered in this paper. Our presentation is slightly more general than most treatments, e.g. [16]; namely we do not assume an additive noise structure in the observational error or suppose that the prior distribution and observation noise are independent.

The problem at hand is to estimate an unknown parameter \mathbf{V} sitting in a separable Hilbert space H and subject to an observational noise η . The forward model is given as

$$\mathcal{Y} = \mathcal{F}(\mathbf{V}, \eta). \quad (\text{C.1})$$

Here $\mathcal{F} : H \times \mathbb{R}^M \rightarrow \mathbb{R}^N$ for possibly different $N, M > 0$ and we assume that \mathcal{F} is a Borel measurable map between the given spaces.⁶ We treat \mathbf{V} and η as random variables on an underlying probability space $(\Omega, \mathcal{A}, \mathbb{P})$. The elements \mathbf{V} and η are distributed as $\mu_0 \in Pr(H)$ and $\gamma_0 \in Pr(\mathbb{R}^M)$ respectively. Note that we will not assume that \mathbf{V} and η are statistically independent in general. In the language of Bayesian statistical inversion, μ_0 is the prior distribution on our unknown parameter \mathbf{V} and γ_0 is the distribution of the measurement noise η . Let $\lambda_0 \in Pr(\mathbb{R}^N)$ denote the distribution of \mathcal{Y} .

We wish to rigorously define the conditional probabilities $\mathcal{Y}|\mathbf{V} = \mathbf{v}$ and $\mathbf{V}|\mathcal{Y} = y$. The former represents the ‘likelihood of an observed data set \mathcal{Y} given $\mathbf{V} = \mathbf{v}$ ’ while the later is ‘the Bayesian posterior distribution for \mathbf{V} given $\mathcal{Y} = y$ ’.

For this purpose we recall some classical definitions around conditional expectations and probabilities from abstract probability theory. For further generalities germane to our discussions here, see e.g. [19, 18].

Definition C.1. *Given a σ -algebra $\mathcal{H} \subseteq \mathcal{A}$ and a random variable Z the conditional expectation of Z given \mathcal{H} denoted $\mathbb{E}(Z|\mathcal{H})$ is the unique (up to a set of measure zero) random variable such that*

$$\mathbb{E}(Z|\mathcal{H}) \text{ is measurable with respect to } \mathcal{H} \quad (\text{C.2})$$

and such that

$$\mathbb{E}(\mathbb{E}(Z|\mathcal{H})\mathbb{1}_A) = \mathbb{E}(Z\mathbb{1}_A) \quad \text{for any } A \in \mathcal{H}. \quad (\text{C.3})$$

Given another random variable W we typically abuse notation and write $\mathbb{E}(Z|W)$ for $\mathbb{E}(Z|\mathcal{H}_W)$ where \mathcal{H}_W is the σ -algebra generated by W . Futhermore, we denote $\mathbb{P}(Z \in A|W) := \mathbb{E}(\mathbb{1}_{Z \in A}|W)$.

We next remind the reader of the definition of a regular conditional distribution as

Definition C.2 (Regular Conditional Distribution). *Consider random variables Z_1, Z_2 taking values in the complete metric spaces (X_1, d_1) and (X_2, d_2) , respectively. We denote the Borel σ -algebra associated with (X_2, d_2) by \mathcal{B}_2 . A regular conditional distribution \mathfrak{J} associated with Z_1, Z_2 is any function $\mathfrak{J} : X_1 \times \mathcal{B}_2 \rightarrow [0, 1]$ such that:*

- (i) *For every $z \in X_1$, $\mathfrak{J}(z, \cdot)$ is a probability measure on \mathcal{B}_2 and, for every $A \in \mathcal{B}_2$, $\mathfrak{J}(\cdot, A)$ is a Borel measurable function on X_1 .*
- (ii) *For each $A \in \mathcal{B}_2$,*

$$\mathfrak{J}(Z_1(\omega), A) = \mathbb{P}(Z_2 \in A|Z_1)(\omega) \quad \text{for almost every } \omega \in \Omega. \quad (\text{C.4})$$

We now define

Definition C.3. *Relative to a given regular conditional distribution \mathfrak{J} , we define the distribution $Z_1|Z_2 = z_2$ rigorously as $\mathfrak{J}(z_2, \cdot)$.*

To clarify these definitions, several remarks are in order.

⁶We could consider the more general case when \mathbb{R}^M and \mathbb{R}^N are replaced by separable Hilbert spaces in what follows. However, we avoid this additional complication for simplicity of presentation and since we are primarily interested situations involving a finite number of observations.

Remark C.4.

- (i) For any two random variables Z_1, Z_2 an associated regular conditional distribution always exists; see [19, Theorem 5.1.9] for a construction.
- (ii) In the case when Z_1, Z_2 take values in \mathbb{R}^n and are jointly, continuously distributed according to the probability density function p , then for any probability density function g ,

$$\mathfrak{I}(z, A) := \begin{cases} \frac{\int_A p(z, w) dw}{\int p(z, w) dw} & \text{if } \int p(z, w) dw > 0, \\ \int_A g(w) dw & \text{otherwise,} \end{cases} \quad (\text{C.5})$$

defines a regular conditional distribution for Z_1, Z_2 .

- (iii) As illustrated by the previous example, regular conditional distributions are not unique in general as the choice of g in (C.5) was arbitrary.

Let us now fix regular conditional distributions

$$\mathbb{Q} : H \times \mathcal{B}(\mathbb{R}^N) \rightarrow [0, 1] \quad (\text{C.6})$$

to define $\mathcal{Y}|\mathbf{V} = \mathbf{v}$ and

$$\mu : \mathbb{R}^N \times \mathcal{B}(H) \rightarrow [0, 1] \quad (\text{C.7})$$

to make sense of $\mathbf{V}|\mathcal{Y} = y$. For more compact notation below we will sometimes write $\mathbb{Q}_{\mathbf{v}}(\cdot) := \mathbb{Q}(\mathbf{v}, \cdot)$ and $\mu_y(\cdot) := \mu(y, \cdot)$.

While we now have a rigorous definition of μ_y we would like to make sense of the usual Bayesian formulation

“posterior distribution \propto likelihood(y) \times prior distribution”

in this general setting. It turns out that all that is needed to derive such a formula is the existence of a distribution γ such that conditional probabilities $\mathbb{Q}_{\mathbf{v}}, \mathbf{v} \in H$ are absolutely continuous with respect to γ .⁷

Proposition C.5. Assume there exists a distribution $\gamma \in Pr(\mathbb{R}^N)$ such that

$$\mathbb{Q}_{\mathbf{v}} \ll \gamma \quad \text{for every } \mathbf{v} \in H \quad (\text{C.8})$$

and suppose that the resulting Radon-Nikodym derivative $\frac{d\mathbb{Q}_{\mathbf{v}}}{d\gamma}(y)$ is measurable in \mathbf{v} and y . Define

$$Z(y, \gamma) := \int_H \frac{d\mathbb{Q}_{\mathbf{v}}}{d\gamma}(y) \mu_0(d\mathbf{v}). \quad (\text{C.9})$$

Then, for any $\tilde{\mu} \in Pr(H)$,

$$\mu_y(d\mathbf{v}) = \mu(y, d\mathbf{v}) := \begin{cases} \frac{1}{Z(y, \gamma)} \frac{d\mathbb{Q}_{\mathbf{v}}}{d\gamma}(y) \mu_0(d\mathbf{v}), & \text{if } Z(y, \gamma) > 0 \\ \tilde{\mu}(d\mathbf{v}), & \text{otherwise,} \end{cases} \quad (\text{C.10})$$

defines a regular condition distribution for $\mathbf{V}|\mathcal{Y} = y$ in the sense of Definition C.3.

Before turning to the proof we make the following simple observation

Lemma C.6. For any bounded and measurable $\psi : \mathbb{R}^N \rightarrow \mathbb{R}$,

$$\mathbb{E}\psi(\mathcal{Y}) = \int_{\mathbb{R}^N} \psi(y) \lambda_0(dy) = \int_H \int_{\mathbb{R}^N} \psi(y) \mathbb{Q}(\mathbf{v}, dy) \mu_0(d\mathbf{v}), \quad (\text{C.11})$$

where λ_0 is the distribution of \mathcal{Y} defined by (C.1) and \mathbb{Q} is the regular conditional distribution (C.6).

⁷Recall that a probability distribution ρ is absolutely continuous with respect to another distribution $\tilde{\rho}$ if $\rho(A) = 0$ whenever $\tilde{\rho}(A) = 0$. We typically denote this relationship by $\rho \ll \tilde{\rho}$.

Proof. Notice that

$$\begin{aligned}\mathbb{P}(\mathcal{Y} \in B) &= \mathbb{E}\mathbb{1}_{\mathcal{Y} \in B} = \mathbb{E}(\mathbb{E}(\mathbb{1}_{\mathcal{Y} \in B} | \mathbf{V})) = \mathbb{E}\mathbb{Q}(\mathbf{V}, B) = \int_H \mathbb{Q}(\mathbf{v}, B) \mu_0(d\mathbf{v}) \\ &= \int_H \int_{\mathbb{R}^N} \chi_B(y) \mathbb{Q}(\mathbf{v}, dy) \mu_0(d\mathbf{v}).\end{aligned}$$

Thus, by linearity we have shown (C.11) for simple functions ϕ . We can now extend to the general case by a standard density argument. \square

We turn now to

Proof of Proposition C.5. We need to verify that μ_y given by (C.10) satisfies the conditions for Definition C.1. The regularity properties in (i) are immediate from the given assumptions on $\frac{d\mathbb{Q}_{\mathbf{v}}}{d\gamma}$. We verify (ii) by showing that, cf. (C.3),

$$\mathbb{E}\left(\int_H \phi(\mathbf{v}) \mu(\mathcal{Y}, d\mathbf{v}) \mathbb{1}_{\mathcal{Y} \in B}\right) = \mathbb{E}(\phi(\mathbf{V}) \mathbb{1}_{\mathcal{Y} \in B}) \quad (\text{C.12})$$

for any $B \in \mathcal{B}(\mathbb{R}^N)$, and any bounded and measurable $\phi : H \rightarrow \mathbb{R}$. Using elementary properties of conditional expectations (see [19, Chapter 5]), recalling the definition of \mathbb{Q} in (C.6), and finally using (C.8) we have

$$\begin{aligned}\mathbb{E}(\phi(\mathbf{V}) \mathbb{1}_{\mathcal{Y} \in B}) &= \mathbb{E}(\mathbb{E}(\phi(\mathbf{V}) \mathbb{1}_{\mathcal{Y} \in B} | \mathbf{V})) = \mathbb{E}(\phi(\mathbf{V}) \mathbb{E}(\mathbb{1}_{\mathcal{Y} \in B} | \mathbf{V})) = \mathbb{E}(\phi(\mathbf{V}) \mathbb{Q}(\mathbf{V}, B)) \\ &= \int_H \phi(\mathbf{v}) \mathbb{Q}(\mathbf{v}, B) \mu_0(d\mathbf{v}) = \int_H \phi(\mathbf{v}) \int_{\mathbb{R}^N} \chi_B(y) \mathbb{Q}(\mathbf{v}, dy) \mu_0(d\mathbf{v}) \\ &= \int_H \phi(\mathbf{v}) \int_{\mathbb{R}^N} \chi_B(y) \frac{d\mathbb{Q}_{\mathbf{v}}}{d\gamma}(y) \gamma(dy) \mu_0(d\mathbf{v}) \\ &= \int_{\mathbb{R}^N} \chi_B(y) \int_H \phi(\mathbf{v}) \frac{d\mathbb{Q}_{\mathbf{v}}}{d\gamma}(y) \mu_0(d\mathbf{v}) \gamma(dy).\end{aligned}$$

On the other hand, we can show

$$Z(y, \gamma) \int_H \phi(\mathbf{v}) \mu(y, d\mathbf{v}) = \int_H \phi(\mathbf{v}) \frac{d\mathbb{Q}_{\mathbf{v}}}{d\gamma}(y) \mu_0(d\mathbf{v}), \quad (\text{C.13})$$

for any $y \in \mathbb{R}^N$. When $Z(y, \gamma) > 0$, (C.13) is true by definition of μ (see (C.10)), and when $Z(y, \gamma) = 0$, we have $\frac{d\mathbb{Q}_{\mathbf{v}}}{d\gamma}(y) = 0$ μ_0 -almost surely (see (C.9)), so both sides of (C.13) are zero. Therefore, by combining the previous two identities and recalling (C.9) we find

$$\begin{aligned}\mathbb{E}(\phi(\mathbf{V}) \mathbb{1}_{\mathcal{Y} \in B}) &= \int_{\mathbb{R}^N} \chi_B(y) Z(y, \gamma) \int_H \phi(\mathbf{v}) \mu(y, d\mathbf{v}) \gamma(dy) \\ &= \int_{\mathbb{R}^N} \int_H \chi_B(y) \int_H \phi(\mathbf{v}) \mu(y, d\mathbf{v}) \frac{d\mathbb{Q}_{\mathbf{u}}}{d\gamma}(y) \mu_0(d\mathbf{u}) \gamma(dy) \\ &= \int_H \int_{\mathbb{R}^N} \chi_B(y) \int_H \phi(\mathbf{v}) \mu(y, d\mathbf{v}) \mathbb{Q}(\mathbf{u}, dy) \mu_0(d\mathbf{u}).\end{aligned} \quad (\text{C.14})$$

Taking $\psi(y) = \chi_B(y) \int_H \phi(\mathbf{v}) \mu(y, d\mathbf{v})$ in (C.11) and combining this identity with (C.14) now finally yields (C.12), completing the proof. \square

Acknowledgments

This work was supported in part by the National Science Foundation under grants DMS-1313272 (NEGH), DMS-1816551 (NEGH), DMS-1522616 (JTB), and DMS-1819110 (JTB); the National Institute for Occupational Safety and Health under grant 200-2014-59669 (JTB); and the Simons Foundation under grant 515990 (NEGH). We would also like to thank the Mathematical Sciences Research Institute, the Tulane University

Math Department, and the International Centre for Mathematical Sciences (ICMS) where significant portions of this project were developed and carried out. The Society for Industrial and Applied Mathematics (SIAM) and NSF grant DMS-1613965, NSF grant 1700124, and the Virginia Tech Interdisciplinary Center for Applied Math (ICAM), respectively, provided funds for travel to the 2016 Gene Golub SIAM Summer School, 2016 FOMICS Winter School on Uncertainty Quantification, and 2017 ICMS workshop Probabilistic Perspectives in Nonlinear Partial Differential Equations, where JK presented the preliminary results of this work and received valuable feedback. We would also like to thank G. Didier, J. Foldes, S. McKinley, C. Pop, G. Richards, G. Simpson, A. Stuart, and J. Whitehead for many useful discussions and thoughtful feedback on this work. The authors acknowledge Advanced Research Computing at Virginia Tech⁸ for providing computational resources and technical support that have contributed to the results reported within this paper.

References

- [1] Volkan Akçelik, George Biros, Omar Ghattas, Kevin R Long, and Bart van Bloemen Waanders. A variational finite element method for source inversion for convective–diffusive transport. *Finite Elements in Analysis and Design*, 39(8):683–705, 2003.
- [2] Marco Baiesi and Christian Maes. Enstrophy dissipation in two-dimensional turbulence. *Physical Review E*, 72(5):056314, 2005.
- [3] Alexandros Beskos, Mark Girolami, Shiwei Lan, Patrick E Farrell, and Andrew M Stuart. Geometric MCMC for infinite-dimensional inverse problems. *Journal of Computational Physics*, 335:327–351, 2017.
- [4] Alexandros Beskos, Frank J Pinski, Jesús María Sanz-Serna, and Andrew M Stuart. Hybrid Monte Carlo on Hilbert spaces. *Stochastic Processes and their Applications*, 121(10):2201–2230, 2011.
- [5] Alexandros Beskos, Gareth Roberts, and Andrew Stuart. Optimal scalings for local Metropolis–Hastings chains on non-product targets in high dimensions. *The Annals of Applied Probability*, 19(3):863–898, 2009.
- [6] Alexandros Beskos, Gareth Roberts, Andrew Stuart, and Jochen Voss. MCMC methods for diffusion bridges. *Stochastics and Dynamics*, 8(03):319–350, 2008.
- [7] Alexandros Beskos and Andrew Stuart. MCMC methods for sampling function space. In *Invited Lectures, Sixth International Congress on Industrial and Applied Mathematics, ICIAM07, Editors Rolf Jeltsch and Gerhard Wanner*, pages 337–364, 2009.
- [8] Jeff Bezanson, Alan Edelman, Stefan Karpinski, and Viral B Shah. Julia: A fresh approach to numerical computing. *SIAM Review*, 59(1):65–98, 2017.
- [9] Jeff Borggaard, Nathan Glatt-Holtz, and Justin Krometis. On Bayesian consistency for flows observed through a passive scalar. *arXiv preprint arXiv: 1809.06228 (Submitted for publication)*, 2018.
- [10] Jeff Borggaard, Nathan Glatt-Holtz, and Justin Krometis. GPU-Accelerated Particle Methods for Evaluation of Sparse Observations for Inverse Problems Constrained by Diffusion PDEs. *Journal of Computational Physics*, 2019.
- [11] Nawaf Bou-Rabee and Jesús María Sanz-Serna. Geometric integrators and the Hamiltonian Monte Carlo method. *Acta Numerica*, 27:113–206, 2018.
- [12] C. Canuto, M.Y. Hussaini, A. Quarteroni, and T.A. Zang. *Spectral Methods: Fundamentals in Single Domains*. Scientific Computation. Springer Berlin Heidelberg, 2007.
- [13] Shiyi Chen and Robert H Kraichnan. Simulations of a randomly advected passive scalar field. *Physics of Fluids*, 10(11), 1998.
- [14] Simon L Cotter, Gareth O Roberts, Andrew M Stuart, and David White. MCMC methods for functions: modifying old algorithms to make them faster. *Statistical Science*, 28(3):424–446, 2013.
- [15] Edward Lansing Cussler. *Diffusion: Mass Transfer in Fluid Systems*. Cambridge University Press, 2009.
- [16] Masoumeh Dashti and Andrew M Stuart. The Bayesian approach to inverse problems. *Handbook of Uncertainty Quantification*, pages 311–428, 2017.
- [17] Simon Duane, Anthony D Kennedy, Brian J Pendleton, and Duncan Roweth. Hybrid Monte Carlo. *Physics letters B*, 195(2):216–222, 1987.
- [18] Richard M Dudley. *Real Analysis and Probability*. Chapman and Hall/CRC, 2018.
- [19] Rick Durrett. *Probability: theory and examples*. Cambridge University Press, 2010.
- [20] Andreas Eberle. Error bounds for Metropolis–Hastings algorithms applied to perturbations of Gaussian measures in high dimensions. *The Annals of Applied Probability*, 24(1):337–377, 2014.
- [21] Andrew Gelman, John B Carlin, Hal S Stern, David B Dunson, Aki Vehtari, and Donald B Rubin. *Bayesian Data Analysis*. CRC Press, third edition, 2014.

⁸<http://www.arc.vt.edu>

- [22] Mark Girolami and Ben Calderhead. Riemann manifold Langevin and Hamiltonian Monte Carlo methods. *Journal of the Royal Statistical Society: Series B (Statistical Methodology)*, 73(2):123–214, 2011.
- [23] David Gottlieb and Steven A. Orszag. *Numerical Analysis of Spectral Methods: Theory and Applications*. CBMS-NSF Regional Conference Series in Applied Mathematics. Society for Industrial and Applied Mathematics, 1977.
- [24] Martin Hairer and Jonathan C Mattingly. Spectral gaps in Wasserstein distances and the 2D stochastic Navier-Stokes equations. *The Annals of Probability*, pages 2050–2091, 2008.
- [25] Martin Hairer and Jonathan C Mattingly. Yet another look at Harris’ ergodic theorem for Markov chains. In *Seminar on Stochastic Analysis, Random Fields and Applications VI*, pages 109–117. Springer, 2011.
- [26] Martin Hairer, Jonathan C Mattingly, and Michael Scheutzow. Asymptotic coupling and a general form of Harris’ theorem with applications to stochastic delay equations. *Probability Theory and Related Fields*, 149(1-2):223–259, 2011.
- [27] Martin Hairer, Andrew M Stuart, and Sebastian J Vollmer. Spectral gaps for a Metropolis–Hastings algorithm in infinite dimensions. *The Annals of Applied Probability*, 24(6):2455–2490, 2014.
- [28] W Keith Hastings. Monte Carlo sampling methods using Markov chains and their applications. *Biometrika*, 57(1):97–109, 1970.
- [29] Michael Hinze, René Pinnau, Michael Ulbrich, and Stefan Ulbrich. *Optimization with PDE Constraints*, volume 23 of *Mathematical Modelling: Theory and Applications*. Springer, New York, 2009.
- [30] Matthew D Hoffman and Andrew Gelman. The no-u-turn sampler: Adaptively setting path lengths in Hamiltonian Monte Carlo. *Journal of Machine Learning Research*, 15(1):1593–1623, 2014.
- [31] Jari Kaipio and Erkki Somersalo. *Statistical and Computational Inverse Problems*, volume 160 of *Applied Mathematical Sciences*. Springer Science & Business Media, 2005.
- [32] G. K. Karch, F. Sadlo, D. Weiskopf, C. D. Hansen, G. S. Li, and T. Ertl. Dye-Based Flow Visualization. *Computing in Science Engineering*, 14(6):80–86, Nov 2012.
- [33] Hamid Kellay and Walter I Goldburg. Two-dimensional turbulence: a review of some recent experiments. *Reports on Progress in Physics*, 65(5):845–894, 2002.
- [34] SC Kou, Qing Zhou, and Wing Hung Wong. Equi-energy sampler with applications in statistical inference and statistical mechanics. *The Annals of Statistics*, 34(4):1581–1619, 2006.
- [35] Robert H Kraichnan. Inertial ranges in two-dimensional turbulence. *The Physics of Fluids*, 10(7):1417–1423, 1967.
- [36] Robert H Kraichnan. Small-scale structure of a scalar field convected by turbulence. *The Physics of Fluids*, 11(5):945–953, 1968.
- [37] Robert H Kraichnan. Stochastic modeling of isotropic turbulence. In *New Perspectives in Turbulence*, pages 1–54. Springer, 1991.
- [38] Justin Krometis. *A Bayesian Approach to Estimating Background Flows from a Passive Scalar*. PhD thesis, Virginia Polytechnic Institute and State University, 2018.
- [39] Antti Kupiainen. Statistical theories of turbulence, 2000. Lectures given at the workshop *Random media 2000*.
- [40] Jonathan C Mattingly, Natesh S Pillai, and Andrew M Stuart. Diffusion limits of the random walk Metropolis algorithm in high dimensions. *The Annals of Applied Probability*, 22(3):881–930, 2012.
- [41] Nicholas Metropolis, Arianna W Rosenbluth, Marshall N Rosenbluth, Augusta H Teller, and Edward Teller. Equation of state calculations by fast computing machines. *The Journal of Chemical Physics*, 21(6):1087–1092, 1953.
- [42] Sean P Meyn and Richard L Tweedie. Markov chains and stochastic stability. Communication and control engineering series. *Springer-Verlag London Ltd., London*, 1:993, 1993.
- [43] Keith W Morton. *Numerical Solution of Convection-Diffusion Problems*. Chapman & Hall, 1996.
- [44] Natesh S Pillai, Andrew M Stuart, and Alexandre H Thiéry. Optimal scaling and diffusion limits for the Langevin algorithm in high dimensions. *The Annals of Applied Probability*, 22(6):2320–2356, 2012.
- [45] Gareth O Roberts and Jeffrey S Rosenthal. Optimal scaling for various Metropolis-Hastings algorithms. *Statistical Science*, 16(4):351–367, 2001.
- [46] James C Robinson. *Infinite-dimensional Dynamical Systems: An Introduction to Dissipative Parabolic PDEs and the Theory of Global Attractors*, volume 28. Cambridge University Press, 2001.
- [47] Boris I Shraiman and Eric D Siggia. Scalar turbulence. *Nature*, 405(6787):639–646, 2000.
- [48] Alexander J Smits. *Flow Visualization: Techniques and Examples*. World Scientific, 2012.
- [49] Andrew M Stuart. Inverse problems: a Bayesian perspective. *Acta Numerica*, 19:451–559, 2010.
- [50] Martin Stynes. Numerical methods for convection-diffusion problems or the 30 years war. *arXiv preprint arXiv:1306.5172*, 2013.
- [51] Roger Temam. *Navier-Stokes Equations and Nonlinear Functional Analysis*, volume 66. SIAM, 1995.
- [52] Luke Tierney. A note on Metropolis-Hastings kernels for general state spaces. *Annals of Applied Probability*, pages 1–9, 1998.

- [53] Sebastian J Vollmer. Dimension-independent MCMC sampling for inverse problems with non-Gaussian priors. *SIAM/ASA Journal on Uncertainty Quantification*, 3(1):535–561, 2015.
- [54] Zellman Warhaft. Passive scalars in turbulent flows. *Annual Review of Fluid Mechanics*, 32(1):203–240, 2000.
- [55] Benjamin S Williams, D Marteau, and Jerry P Gollub. Mixing of a passive scalar in magnetically forced two-dimensional turbulence. *Physics of Fluids*, 9(7):2061–2080, 1997.
- [56] Merzkirch Wolfgang. Flow visualization. *Academic Press (LONDON) LTD*, 1987.
- [57] Sergiy Zhuk, Tigran T Tchrakian, Stephen Moore, Rodrigo Ordóñez-Hurtado, and Robert Shorten. On Source-Term Parameter Estimation for Linear Advection-Diffusion Equations with Uncertain Coefficients. *SIAM Journal on Scientific Computing*, 38(4):A2334–A2356, 2016.

Jeff Borggaard

Department of Mathematics

Virginia Tech

Web: <https://www.math.vt.edu/people/jborggaa/>

Email: jborggaard@vt.edu

Justin Krometis

Advanced Research Computing

Virginia Tech

Web: <https://www.arc.vt.edu/justin-krometis/>

Email: jkrometis@vt.edu

Nathan Glatt-Holtz

Department of Mathematics

Tulane University

Web: <http://www.math.tulane.edu/~negh/>

Email: negh@tulane.edu